Journal of Advanced Transportation

Ecodriving Strategies for Autonomous Electric Transportation Systems

Lead Guest Editor: Cherif Larouci
Guest Editors: Xiaobo Qu and Umberto Papa

Ecodriving Strategies for Autonomous Electric Transportation Systems

Journal of Advanced Transportation

Ecodriving Strategies for Autonomous Electric Transportation Systems

Lead Guest Editor: Cherif Larouci
Guest Editors: Xiaobo Qu and Umberto Papa

Contents

Hindawi
Journal of Advanced Transportation
Volume 2020, Article ID 1840975, 17 pages
https://doi.org/10.1155/2020/1840975

Research Article

Personal Characteristics of e-Bike Riders and Illegal Lane Occupation Behavior

Changxi Ma[1], **Jibiao Zhou**[2,3], **Dong Yang**[1], **Fuquan Pan**[4], **and Yuanyuan Fan**[1]

[1]*School of Traffic and Transportation, Lanzhou Jiaotong University, Anning West Rd. #88, Anning District, Lanzhou 730070, China*
[2]*Department of Transportation Engineering, Tongji University, Caoan Rd. #4800, Shanghai 201804, China*
[3]*Intelligent Transport System (ITS) R&D Center, Shanghai Urban Construction Design and Research Institute (Group) Co., Ltd., Dongfang Rd. #3447, Pudong New Area, Shanghai 200125, China*
[4]*School of Mechanical and Automotive Engineering, Qingdao University of Technology, Changjiang Middle Rd. #2, Qingdao 266520, China*

Correspondence should be addressed to Changxi Ma; machangxi@mail.lzjtu.cn and Jibiao Zhou; zhoujibiao@tongji.edu.cn

Received 14 July 2019; Revised 19 December 2019; Accepted 9 June 2020; Published 27 June 2020

Academic Editor: Cherif Larouci

This study aimed to reveal the potential relationship between personal characteristics of e-bike riders and illegal occupation of motor vehicle lane. To this end, a questionnaire survey was conducted and 350 valid copies of responses were retrieved from the e-bike riders. Depending on the number of motor vehicle lanes occupied, the risky behavior of illegal occupation was divided into four intervals: intervals A, B, C, and D. The disaggregate theory has high adaptability to the analysis of individual traffic behavior. In this study, the multinomial logit model was used, and eight personal characteristics of e-bike riders were selected. The aforementioned four intervals were the four selection limbs, and a measurement model calculating the influence of personal characteristics on the behavior of illegal occupation was built. The theory of elasticity was employed to analyze the sensitivity degree of each influence factor. The results showed that the absolute values of elasticity of all tested influence factors, including age, educational level, and eye vision, were less than 1.000. However, on the four intervals, the elasticity of riders' temperament was 1.203, 1.656, 1.554, and 1.355, respectively, and elasticity of riding proficiency was 2.782, 3.883, 3.453, and 2.932, respectively.

1. Introduction

e-bike is defined as the mass of the whole vehicle shall not exceed 55 kg, the speed shall not exceed 25 km/h, and the motor power shall be 400 W. It strengthens the requirements of riding ability and must have foot riding device, tamper proof, fire-retardant device, waterproof ability, charging protection device, etc. [1].

In recent years, many large- and medium-sized cities of China have witnessed the growing prevalence of e-bikes for daily transport due to their low cost, convenience, and flexibility of riding [1–4]. Unlike North America and Europe, the e-bike has already become one of the most popular modes of transportation, for example, for daily commuting, and not for leisure only. The China Bicycle Association [5], in 2017, reported that e-bike ownership in China amounted to 250 million. The annual production of e-bikes was 30.97 million, and the export volume was 7.301 million with an export value of US $1.44 billion. In some cities, such as Nanning, Haikou, Kunming, and Guilin, the number of e-bikes has far exceeded that of conventional bikes [1, 3–5]. For example, e-bikes in the urban area of Nanning amounted to more than 1.8 million [6]. Nanning is the Chinese city with the greatest number of e-bikes and hence known as the city on an e-bike. Apparently, the e-bike has already become an important commuting tool [7, 8].

In spite of this, the rapid increase in the number of e-bikes has given rise to a series of safety problems. Besides conventional bike riders and pedestrians, e-bike riders are also a disadvantaged group. Because of their fast traveling

speed, e-bikes also have a high risk of serious accidents. According to the 2015 China Statistical Yearbook on Road Traffic Accidents, the number of e-bike accidents was 8.2-fold that of bike accidents and 5.4-fold that of pedestrian accidents [9, 10]. From January to June 2016, the number of e-bike accidents in Jiangsu accounted for 70% of the national total [11]. Further, data on hospital admissions related to e-bike accidents are also bleak. As indicated by hospitalization records of e-bike riders in Hefei from 2009 to 2011, one-third of the e-bike riders were seriously wounded [1, 2, 12]. According to the hospitalization records of Suzhou from October 2010 to April 2011, the number of people injured during e-bike accidents accounted for 57.2% of all hospital admissions due to road traffic accidents [12]. Both the seriousness and the number of e-bike accidents have increased. According to statistics [13, 14], the number of deaths due to e-bikes nationwide was 73 and 1305 in 2011 and 2016, respectively, indicating an increase by 78.02% in 5 years. The number of people injured during e-bike accidents was 8532 and 16,944, respectively, which was an increase by 14.71%. Given such frequency and seriousness, Guangzhou, Shenzhen, Wenzhou, and Fuzhou have banned or restricted the use of e-bikes [3, 4, 8, 10, 14–18]. Based on the statistical analysis of accident data and causes, Ren et al. [17] proposed a classification into 12 risky behaviors of riding: illegal occupation of lanes, riding in the opposite direction, riding through a red light, riding overspeed, riding while drunk, turning around the corner at a fast speed, crossing the road abruptly, riding in parallel, riding while making telephone calls, riding with music on, riding while chatting, and riding with someone else on the bike. The results showed that illegal occupation of lanes and riding with someone else on the bike were associated with the highest probability of traffic accident.

The safety problem of e-bike riding has drawn increasing attention, necessitating the need to understand the relationship between personal characteristics of e-bike riders and risky behaviors of riding, especially the relationship between personal characteristics and illegal occupation of lanes. The present study attempted to reduce the occurrence probability of e-bike accidents and raise the safety awareness of e-bike riders. The results shed some light on improving road traffic safety and reducing road traffic accidents.

2. Literature Review

Questionnaire survey [1–3, 18–28] and video capture [16, 29–32] were the two most commonly used methods in this study to collect data on risky behaviors of e-bike riding. The questionnaires were usually designed based on the previous behavioral studies of light motorcycle and motorcycle riders and car drivers. Most of the research programs use light motorcycle rider behavior questionnaire designed by Yao and Wu [18], motorcycle rider behavior questionnaire designed by Steg and Brussel [22], and Chinese riding behavior questionnaire designed by Elliott et al. [23]:

(1) The questionnaire survey approach has been widely used in traffic safety studies for collecting information about the riding behavior, safety attitude, and risk perception [18, 21–28]. For example, Ma et al. [21] examined the relationship between electric bike riders' individual characteristics and their riding speed using a questionnaire-based method. Yao and Wu [18] studied the risk factors involved in e-bike accidents based on the questionnaire survey and determined the relationship between safety attitude, risk perception, and aberrant riding behavior. Steg and Brussel [22] developed a light motorcycle rider behavior questionnaire and confirmed the distinctions between wrong, faulty, and illegal behaviors of light motorcycle riders in Holland. Elliott et al. [23] developed motorcycle driver behavior questionnaire (DBQ) and identified the differences between Britain's traffic errors, control errors, speed violation, and stunt and safe use of motorcycle. Similar studies have also been found in [24–27]. Reason et al. [28] proposed the logical framework for assessing aberrant riding behaviors and designed the DBQ, which differentiated between three types of behaviors: wrong behavior (failure of planned action to achieve the desired effect), mistaken behavior (deviation of behavioral intention from intention), and illegal behavior (intentional deviation from normal safe behavior or socially recognized code of conduct). The revised versions of DBQ have also been used to study aberrant behaviors of two-wheeled vehicle riders, for example, motorcycle riders and light motorcycle riders.

(2) The video capture approach uses the electronic monitoring devices on road and observes the riding behaviors and features of e-bike riders. This method was featured by the massiveness of data. Zhou et al. [16] employed Global Eyes Network video monitoring technology of China Telecom to acquire real-time video data of e-bikes in Ningbo. The major factors influencing the waiting endurance time of e-bike riders were observed. It was found that weather, with or without a pedestrian crosswalk, and law enforcement by traffic police had the largest influence. Konstantina [29] observed 90,000 e-bike riders at 6 monitoring sites in Iowa and studied the influence of road conditions, geographical position, and weather on the use of helmet among riders. Truong et al. [30] observed 26,000 motorcycle and e-bike users and concluded that the use of cell phone while riding correlated to motorcycle type and age. Huan et al. [31] used video monitoring data at road intersections to establish a model that analyzed the factors influencing the waiting endurance time and red-light running behavior of e-bike riders at the intersections. They found that the smaller the number of e-bike riders or the larger the number of motor vehicles at the intersection, the lower the frequency of red-light running behavior among the

riders. Du et al. [32] performed an observation of 18,000 e-bike riders at intersections in Suzhou and summarized the risky riding behavior.

Many risky riding behaviors are seen among e-bike riders. Traffic violation behaviors are prevalent among e-bike riders. Aberrant riding behaviors usually include the illegal occupation of lanes (Figure 1), overspeeding, red-light running, riding in an opposite direction, and riding with someone else on the e-bike. For example, Du et al. [12] focused on the riding behavior of e-bike riders and reported that riding with someone else on the e-bike, illegal occupation of lanes, red-light running, riding in an opposite direction, and making phone calls while riding were risky riding behaviors. Zhao et al. [33] investigated the risky riding behaviors of e-bike riders and conducted a 4-day survey in Jinhua, China. The results showed that overspeeding, riding with someone else on the e-bike, red-light running, and riding in the opposite direction were among the major risky riding behaviors. Wu et al. [34] investigated the relationship between riding behavior, age, and gender based on the survey data. It was found that young and middle-aged adults were more prone to red-light running compared with elderly people and that male had a higher probability of red-light running compared with female. This was especially true among male riders of battery vehicles with higher dynamic performance. Schepers et al. [35] showed that the seriousness of e-bike accidents far exceeded that of ordinary bike accidents.

Moreover, after correction for riders' age, gender, and bike use frequency, e-bike riders were more likely to be involved in a serious traffic accident. Petzoldt et al. [36] studied the differences between ordinary bikes and e-bikes in traffic conflicts through 80 volunteers. Insignificant differences were reported between the two, but at the intersections, the number of traffic conflicts involving e-bikes was twice that of ordinary bikes. Moreover, the traveling speed was higher for e-bikes upon traffic conflict, and the probability of traffic accidents was also higher. e-Bike riders are an emerging traffic population, and it takes more time for other road users to get used to it. Johnson and Rose [37] performed an online survey on e-bike use among elderly people aged more than 65 years in Australia. It was found that elderly people were more familiar with the safety knowledge of e-bike use and riding and that 84.1% of elderly riders did not get involved in any e-bike accidents. Hu et al. [15] discussed the factors influencing e-bike traffic accidents in Hefei. The results showed that riders' age, gender, and type of e-bike had a significant impact on traffic accidents. Cherry et al. [38] analyzed the illegal behaviors of e-bike riders and found that overspeeding, red-light running, and overloading were also the major causes of traffic accidents. Moreover, the high frequency of e-bike traffic accidents was closely related to losing control on e-bikes while getting onto the road. For example, Xing et al. [39] performed a roadside observation of risky behaviors of e-bike riders in a city in Anhui province. They found that riders had an average traveling speed of 24 km/h at different time intervals within a day and that 74.60% of riders had a traveling speed of more than 20 km/h. Zhou et al. [16] studied e-bikes crossing the intersections illegally at a red light. The influence was analyzed. The results showed that three factors, namely, weather, length of a pedestrian crosswalk, and no law enforcement by traffic police, had the greatest influence on the waiting endurance time.

Taken together, extensive studies [1–3, 18, 21, 40–43] have been conducted on riding behaviors of e-bike riders, which contribute to the riding safety of e-bikes. However, fewer studies have been carried out concerning the relationship between personal characteristics of e-bike riders and risky riding behaviors, especially illegal occupation of lanes. However, many traffic accidents are caused by the illegal occupation of lanes by e-bike riders, and such behavior poses a great threat to life and property safety of the riders [12, 18, 21, 31, 33, 44]. This study analyzed whether personal characteristics of riders were directly related to illegal occupation of lanes. The disaggregate theory was used, and a measurement model for assessing the influence of each personal characteristic of riders on illegal occupation of lanes was established. The relationship between each influencing factor and illegal occupation of lanes was quantified, and sensitivity analysis was performed. By conducting a systematic study on the influence degree and mechanism, the influence of personal psychology and psychological properties of riders on the riding behaviors was analyzed from the perspective of traffic psychology. This study can enrich the systematic theory on e-bike riders and lay a theoretical basis for curbing the behavior of illegal occupation of lanes. This will further promote the riding safety and efficiency of e-bike riders.

3. Data Collection and Processing

3.1. Data Collection

3.1.1. Survey Design. A questionnaire on personal characteristics of e-bike riders was designed. Then, with the help from traffic police, data were collected by field sampling. The specific process was as follows: the traveling speed of the samples (i.e., e-bike riders) was acquired with a radar speed detector. Then, in the downstream road section 200 m away, the e-bike rider was stopped with the help of traffic police. This rider was then informed of the purpose of the questionnaire survey and received the questionnaire. If the rider was not cooperative, the sample was dropped. The road sections surveyed were two-way six-lane roads; bus stops and intersections were avoided to reduce the influence of other traffic-related factors on e-bike riders. The actual road conditions and the length of road section chosen from the survey are shown in Figure 2.

Demographic information included sex, age, driving age, and educational level. Participants were also asked to report their character, occupation, riding proficiency, and eye vision.

3.1.2. Speed Selection Behavior. According to the requirements in the safety technical specification for electric bicycle

(a) (b)

Figure 1: Riding behavior of illegal occupation (IO). (a) One e-bike involves IO. (b) Multiple e-bikes involve IO.

(a) (b)

Figure 2: Actual road conditions and the length of road section chosen for the survey. (a) Actual road conditions. (b) Length of road section.

[45], the traveling speed of e-bikes of more than 25 km/h on an urban road was considered as overspeed. Thus, the speed limit for choosing the overspeeding of samples was set as 25 km/h. To more reasonably study the influence of personal characteristics of riders on their behavior of illegal occupation of lanes based on survey data, the lanes occupied were divided into four categories: nonmotor vehicle lane, first motor vehicle lane, second motor vehicle lane, and third and higher motor vehicle lane, each one represented by intervals A, B, C, and D, respectively. Thus, the numbers of riders occupying different lanes were calculated. The specific interval division diagram is shown in Table 1. The relationship between riders' personal characteristics, traveling speed, and occupation of motor vehicle lane was discussed using survey data. To do this, the average traveling speed of e-bike riders was acquired for the road section concerned. According to the limit on the traveling speed of e-bike riders and actual distribution of speed data for the road section, the traveling speed of the riders was divided into four intervals, namely, 0–15, 15–25, 25–35, and 35 km/h and above, which were represented by A, B, C, and D, respectively. Using the survey data, the number of riders within each speed interval and average traveling speed were calculated.

Four intervals, A, B, C, and D, corresponding to different lane occupation behaviors, were the four selection limbs of the mode, the values of which were 0, 1, 2, and 3, respectively. The personal characteristics as influencing factors for the selection of lane occupation behavior were assessed and identified, as shown in Table 2.

3.2. Data Processing. The subjects surveyed were e-bike riders, and a total of 352 copies of responses were retrieved. Among these, 350 copies were found to be valid after screening. According to the statistics, 311 were male riders (88%) and 41 were female riders (12%). They were 18–61 years old, and they all had more than 1 year of driving age. Statistics of the personal characteristics of e-bike riders are shown in Table 3.

Table 1: Interval division diagram of road lanes occupied by e-bike riders.

Middle isolation zone	Third motor vehicle lane	Second motor vehicle lane	First motor vehicle lane	Nonmotor vehicle lane
Middle isolation zone	Interval D	Interval C	Interval B	Interval A
Middle isolation zone	35 km/h and above	25–35 km/h	15–25 km/h	0–15 km/h

Table 2: Influencing factors.

Influencing factor	Variable	Explanation
Gender	X_1	1 for male and 0 for female
Age	X_2	Classified into four age groups: 18–30 years, 30–45 years, 45–60 years, and older than 60 years, assigned with values 0, 1, 2, and 3, respectively
Educational level	X_3	Classified into four levels: primary school and lower, junior high school, senior high school, and university and higher, assigned with values 0, 1, 2, and 3, respectively
Driving age	X_4	Classified into four levels: 1 year or less, 1–3 years, 3–5 years, and more than 5 years; the values are 0, 1, 2, and 3, respectively
Character (temperament)	X_5	Classified into four types: melancholic, phlegmatic, sanguineous, and choleric, assigned with values 0, 1, 2, and 3, respectively
Occupation	X_6	Classified into four groups: students, in-service staff, self-employed, and retirees (other), assigned with values 0, 1, 2, and 3, respectively
Vision correction	X_7	Dummy variable: 1 for yes, 0 for no
Cycling proficiency	X_8	Classified into four levels: novice, moderately skilled, skilled, and highly skilled, assigned with values 0, 1, 2, and 3, respectively

Table 3: Statistics of personal characteristics of e-bike riders.

Personal characteristic	Number of e-bike riders							
Gender	Male	310	Female	40				
Age	18–30 years	108	30–45 years	142	45–60 years	81	60 years and more	19
Educational level	Primary school and lower	27	Junior high school	121	Senior high school	157	University and higher	45
Driving age	Below 1 year	21	1–3 years	180	3–5 years	122	5 years and more	27
Character (temperament)	Melancholic	1	Lymphatic	129	Sanguine	149	Bilious	71
Occupation	Student	11	Employee	179	Freelancer	141	Retiree	19
Vision correction	Corrected	284	Not corrected	66				
Riding proficiency	Very skillful	130	Skillful	189	Moderately skillful	25	Novice	6

Data on average traveling speed and specific lanes occupied by the e-bike riders are shown in Tables 4 and 5, respectively.

Table 4: Traveling speed of e-bike riders.

Interval of speed selection	A	B	C	D
Number of riders	10	133	147	60
Average riding speed	13.3037	20.7137	28.8339	40.7376

3.3. Reliability and Validity Tests

3.3.1. Reliability Test. Reliability test can well reflect the reliability of data sources of the questionnaire survey and is considered an indispensable step before formal data analysis. The higher the reliability of the survey data, the more reliable the conclusions drawn from data analysis. The results of reliability test are usually represented by three indicators, namely, Cronbach's alpha, Guttman's coefficient, and split-half coefficient. In the questionnaire used in this study, some items were scored in multiple ways, and so internal consistency of the questionnaire was assessed by Cronbach's α:

$$\alpha = \left(\frac{k}{1-k}\right)\left(1 - \frac{\sum_{i=1}^{k} S_i^2}{S_x^2}\right), \quad (1)$$

where k is the number of items contained in the questionnaire; S_i^2 is the variance of score of the ith item (measured value); and S_x^2 is the variance of the total questionnaire score. The increased content of reliability test is as follows: note that the reliability coefficient is closely related to the number of items (k) of the scale; the more the number of items, the greater the acceptable reliability. For a scale with about 10 questions, if the coefficient of α reaches 0.7, the reliability is good [46].

The SPSS 19.0 software was used to verify the reliability of data from the questionnaire survey. It was found that Cronbach's alpha was more than 0.807 for three potential variables, namely, riding proficiency, occupation, and temperament. The overall reliability of eight variables was 0.722 indicating that the reliability of the questionnaire was good; that is, the questionnaire was acceptable in the overall design.

3.3.2. Validity Test. Validity consists of content validity, criterion validity, and construct validity, and construct

Table 5: Lanes illegally occupied by e-bike riders.

Interval for different lanes occupied	A Nonmotor vehicle lane	B First motor vehicle lane	C Second motor vehicle lane	D Third and higher motor vehicle lane
Number of riders	91	177	49	33

validity is a measure of the degree of agreement between practice and theory. Factor analysis is the most commonly used method for demonstrating construct validity. However, many problems in reality not only involve multiple variables but also intricate connections between the variables. The best way is to extract a few synthetic variables that contain the majority of information in the original variables. Moreover, these synthetic variables should be mutually independent. Factor analysis is an ideal method to derive synthetic variables so that the relationship between multiple variables can be depicted using a few factors. Variables described are usually actually observed random variables, while the synthetic variables are unobservable ones. In actual application, these factors are known as common factors. The personal characteristics of riders identified by the questionnaire survey as related to illegal occupation of lanes were consistent with the common factors found by factor analysis.

The starting point of factor analysis is to represent the majority of the information contained in the original variables by mutually independent variables, which can be expressed by the following mathematical model [46]:

$$\begin{aligned} x_1 &= a_{11}F_1 + a_{12}F_2 + \ldots + a_{1m}F_m, \\ x_2 &= a_{21}F_1 + a_{22}F_2 + \ldots + a_{2m}F_m, \\ &\ldots \\ x_p &= a_{p1}F_1 + a_{p2}F_2 + \cdots + a_{pm}F_m, \end{aligned} \tag{2}$$

where $x_1, x_2, \cdots, x_p$ are p original variables, which are standardized variables with a mean of 0 and standard deviation of 1; $F_1, F_2, \cdots, F_m$ are m factor variables; and m is smaller than p. It can be represented in the following matrix form:

$$X = AF + a\varepsilon, \tag{3}$$

where F is a common factor, representing m mutually perpendicular coordinate axes in the high-dimensional space, and A is the factor load matrix, the load of the ith original variable on the jth factor variable.

The content of the validity test is as follows: the steps of factor analysis are to (1) determine whether the original variables to be analyzed are suitable for factor analysis; (2) construct factor analysis; (3) use rotation method to make factor variables more interpretable; and (4) calculate factor scores.

In the validity test of the questionnaire, the Kaiser–Meyer–Olkin (KMO) measure of sampling adequacy and the Bartlett test for sphericity were performed to determine whether the questionnaire data were fit for factor analysis. The value of KMO measure was 0.689, which was greater than 0.50, and that of Sig was 0.00, which was less than 0.05, indicating that the questionnaire was suitable for factor analysis. Principal component analysis is commonly used for factor analysis to test the construct validity of the questionnaire. Principal common factors were extracted from the questionnaire. Three principal components existed with a characteristic root of greater than 1, and the percentage contribution of these three principal components was 29.194%, 20.376%, and 12.423%, respectively. The cumulative contribution rate was 61.994%, indicating that the potential variables screened through the test had high construct validity.

4. Construction of the Behavior Selection Model and Riding Behavior Selection

4.1. Disaggregate Model. Logit model is a special form of generalized linear regression model. The model itself has few restrictions on data conditions. The independent variable can be continuous variable or unnecessary or orderly classified variable, and the variable is not required to meet the normal distribution. At present, the commonly used logit models are binomial logit regression model, conditional logit regression model, ordered logit regression model, and multiple classified ordered logit regression model. Among them, the ordinal logit model is an extension of binomial logit model, which was proposed by McCullagh in 1980 to analyze the data whose dependent variable is ordinal classified variable. Many studies have found that for classified ordered data, binomial logit model instead of ordered logit model can only achieve 50%–70% of the test efficiency, which shows that multiple classified ordered logit model has a good effect in dealing with classified variable data [23–27].

Individual data were used for model construction and calibration when applying disaggregate theory to analyze individual traffic behaviors. From the 1970s to the present day, a disaggregate model has been widely used in the transportation field and abundant achievements have been made [22–26, 47–51]. It is assumed with the disaggregate model that the travelers may choose the transportation scheme with the maximum utility. The utility function, divided into fixed and random parts, was expressed as follows:

$$U_{in} = V_{in} + \varepsilon_{in}, \tag{4}$$

where

$$V_{in} = \sum_{k=1}^{k} \theta_k X_{ink}, \tag{5}$$

U_{in} is the utility function of the ith scheme chosen by the nth traveler; V_{in} is the fixed term of U_{in}; ε_{in} is the random term of U_{in}; k is the specific number of attribute variables; θ_k is the

parameter value of the kth variable; and X_{ink} is the value of the kth attribute variable of the ith scheme chosen by the nth traveler.

In the aforementioned disaggregate model, when ε_{in} obeyed the double exponential distribution and multivariate normal distribution, the logit and probit models could be built, respectively. e-bike riders as the principal participants in the transportation system usually show traffic selection behaviors that are hard to capture accurately, thus leading to randomness in the changes of the transportation system. When the e-bike riders choose to occupy the motor vehicle lanes, both personal and environmental factors are responsible for shaping such a choice. However, environmental factors exert a similar influence on all riders, while the selection of behavior of illegal lane occupation displays discreteness. This is mainly due to the varying perception about the environmental factors on the part of riders. That is, the riders develop different perception and occupy different lanes even in the same environment. Thus, personal characteristics have the most decisive impact on the behavior of illegal occupation of motor vehicle lanes. Conventional models cannot reflect the double features of discreteness and nonlinearity of riding behaviors stemming from the personal characteristics of the riders. In contrast, the disaggregate model especially targets these features and is highly adaptive in this field. Furthermore, the behavior of occupying motor vehicle lanes is chosen by the riders after comprehensive consideration of multiple factors in an attempt to achieve maximum expected utility. This conforms to the initial assumption of the disaggregate theory. Therefore, a disaggregate model was applied to analyze the riding behavior selection of e-bike riders.

4.2. Construction of Riders' Behavior Selection Model. A riders' illegal lane occupation behavior selection model was constructed based on the multinomial logit (MNL) theory and valid data of personal characteristics of e-bike riders. Based on the basic form of an MNL model, ε_{in} obeyed dual exponential distribution and ε_{in} was V_{in} mutually dependent. Then, the probability of the nth rider choosing the ith behavior of illegal lane occupation was expressed as follows:

$$P_{in} = \frac{e^{V_{in}}}{\sum_{i=1}^{I_n} e^{V_{in}}}, \tag{6}$$

where I_n is the total number of currently optional behaviors; P_{in} is the probability that the nth rider chooses the ith behavior; ε_{in} is the random term of utility function for the nth rider choosing the nth scheme; and V_{in} is the fixed term of utility function U_{in} for the nth rider choosing the ith scheme.

The model construction and calculation workflow based on the basic features of riding behavior selection are shown in Figure 3. In the figure, t is the t-statistic for each influence factor and R^2 is the correlation coefficient.

4.3. Model Solution

4.3.1. Calibration of Influencing Factors of the Model. The SPSS software was used to calibrate the influencing factors of the model. Table 6 shows that the minimum t-statistic (absolute value) was 4.975, which was higher than 1.960, indicating that the influencing factors were significant.

In the statistical analysis using SPSS, R^2 was used to measure the degree of fitness of the model and was called correlation coefficient, where $R^2 \in (0, 1)$. The closer the value of $R^2$to 1.000, the higher the degree of linear regression predictions fitting the data, and the higher the agreement between the built model and actual situation. In this study, the correlation coefficient R^2 was 0.594, and the adjusted value of R^2 was 0.563, as shown in Table 7, indicating good fitness of the model.

4.3.2. Utility Function. Parameter values of each influencing factor on the four intervals are shown in Table 8. According to Table 8, the utility functions V_0, V_1, V_2, and V_3 corresponding to intervals A, B, C, and D were, respectively, as follows:

$$\begin{aligned} V_0 &= 0.491X_1 - 0.059X_3 + 1.030X_5 + 0.417X_6 + 1.919X_8, \\ V_1 &= 0.730X_2 - 0.059X_3 + 0.334X_4 + 1.030X_5 + 0.430X_7, \\ V_2 &= -0.059X_3 + 0.334X_4 + 1.030X_5 + 0.417X_6 + 1.919X_8, \\ V_3 &= 0.491X_1 + 0.730X_2 + 1.030X_5 + 0.430X_7 + 1.919X_8. \end{aligned} \tag{7}$$

To determine the relationship between each influencing factor and behavior of illegal lane occupation among e-bike riders, a sensitivity analysis was performed for each influencing factor. The degree of sensitivity is usually represented by elasticity. In the disaggregate theory, when an influencing factor changes, the elasticity E for variation in the probability of riding scheme selection is given by

$$E = \theta_k X_{ink} (1 - P_{in}). \tag{8}$$

Elasticity can be positive or negative. When the two variables correlate positively, the elasticity value is positive; otherwise, it is negative. The absolute values of all elasticities of more than 1.000 on the four intervals indicate that the influence factor has elasticity on the selection of illegal lane occupation behavior; otherwise, elasticity is lacking. First of all, the means of personal characteristics of riders on each interval were calculated based on the survey data of personal characteristics and illegal lane occupation behavior of the riders. Next, the parameter values obtained in Table 4 were introduced into (5) and (6), and the probability of selecting illegal lane occupation behavior was calculated. Then, using the calculation (8), the elasticity of each influencing factor for the probability of selecting illegal lane occupation behavior was derived.

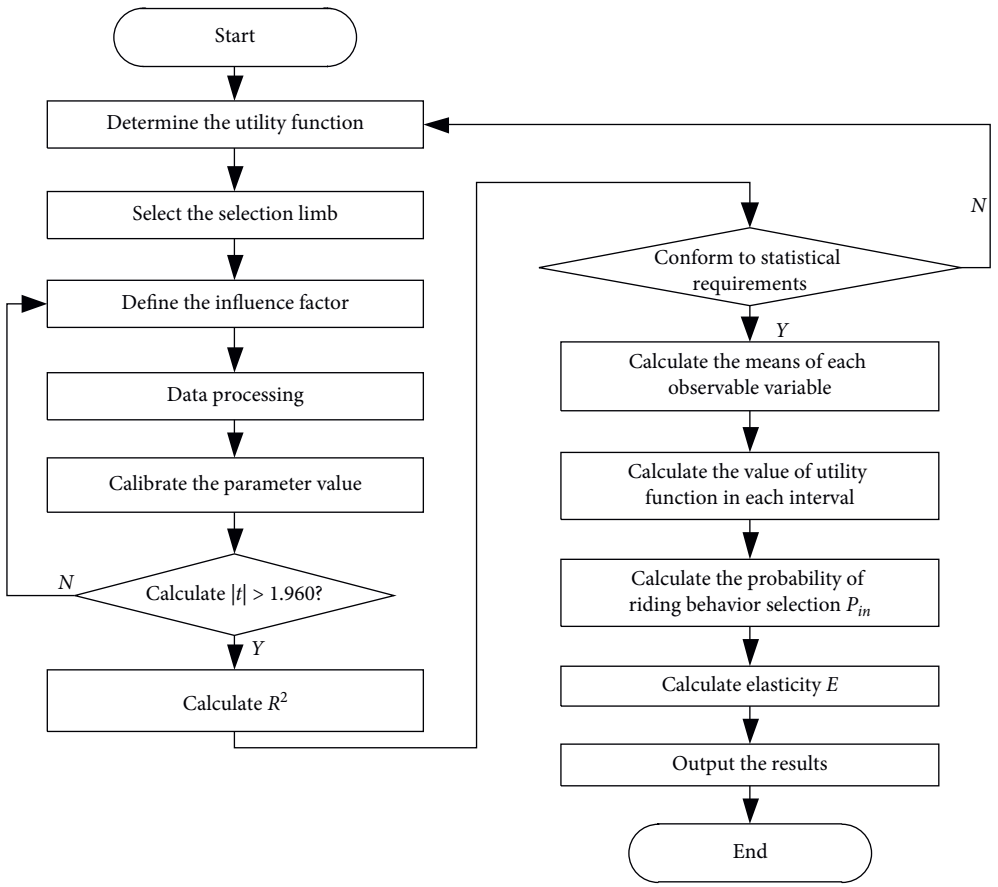

Figure 3: Model calculation workflow.

Table 6: Calibration of influencing factors of the model.

Influencing factor	Variable	Parameter value	Standard deviation	t-Statistic
Gender	X_1	0.491	0.122	16.364
Age	X_2	0.730	0.056	6.946
Educational level	X_3	−0.059	0.060	11.318
Driving age	X_4	0.334	0.066	12.581
Temperament	X_5	1.030	0.056	13.101
Occupation	X_6	0.417	0.062	18.977
Vision correction	X_7	0.430	0.103	4.905
Cycling proficiency	X_8	1.919	0.061	15.619

Table 7: Degree of fitness of the calibrated model.

Model	R	R^2	Adjusted R^2	Standard error of estimate
1	0.771	0.594	0.563	1.769

Table 8: Influencing factors and parameter values.

Influencing factor	Variable	Interval			
		A	B	C	D
Gender	X_1	0.491			0.491
Age	X_2		0.730		0.730
Educational level	X_3	−0.059	−0.059	−0.059	
Driving age	X_4		0.334	0.334	
Character	X_5	1.030	1.030	1.030	1.030
Occupation	X_6	0.417		0.417	
Vision correction	X_7		0.430		0.430
Cycling proficiency	X_8	1.919		1.919	1.919

5. Results Analysis

5.1. Relationship between Personal Characteristics and Illegal Lane Occupation of e-Bike Riders. Different riding habits and behaviors were derived from riders with different personal characteristics. Given limited traffic resources (some nonmotor vehicle lanes occupied by motor vehicle lanes), riders are faced with a shortage of nonmotor vehicle lanes. As a result, many nonmotor vehicle riders tend to occupy motor vehicle lanes, and e-bike riders account for a greater proportion. The personal characteristics identified to influence illegal lane occupation by e-bike riders were gender, age, educational level, driving age, temperament, occupation, and road infrastructure of motor vehicle lanes. Therefore, the personal characteristics of e-bike riders were discussed in this study to shed light on the influence of personal characteristics of riders on their behavior of illegal lane occupation.

5.1.1. Gender and Age. Using the method described in Section 4, the selection probability and parameter value of gender and age on different intervals and the means and elasticity of each influencing factor on each interval were evaluated, as shown in Table 9. Similarly, the values corresponding to each influencing factor were also evaluated using this method. In field sampling, 88% of the e-bike riders were male, while the female riders took up a small proportion of the surveyed area. The probability of illegal lane occupation was more than 0.713, which was higher than 0.500. Apparently, more than one-half of the e-bike riders would choose to occupy the motor vehicle lanes when traveling. As shown in Table 9, the means for gender on the four intervals increased steadily, and all of them were more than 0.921 and 0.500 for male and female, respectively. That is, male riders outnumbered the female riders. In other words, male riders were more likely to occupy motor vehicle lanes compared with female riders. The values of elasticity for gender on the four intervals were all less than 1.000, indicating the lack of elasticity of gender for the choice of illegal lane occupation behavior. However, the elasticity was 0.391 on interval B, which was higher than that on the other three intervals. This indicated that gender had the greatest impact on the behavior of occupying the first motor vehicle lane.

The means for age on the B interval is the highest. This meant people aged between 30 and 45 have the highest probability of choosing the illegal lane occupation behavior. This correlated with the personality traits of young people, such as impulsiveness and lack of safety awareness. Elasticity for age was smaller than 1.000 on the four intervals, indicating that age had a low elasticity on the choice of illegal lane occupation behavior. However, elasticity was the highest on interval B (occupying the first motor vehicle lane), the value being 0.693. This indicated that compared with the other three intervals, age had the most significant impact on the choice of the behavior of occupying the first motor vehicle lane. That is, the younger the age of e-bike riders, the more likely that the riders occupied the motor vehicle lane closer to the middle isolation zone.

5.1.2. Educational Level and Driving Age. Table 10 shows the results on the educational level and driving age. According to the table, the means for the educational level were similar on all the four intervals and changed steadily. The mean was the highest on interval A, the value being 1.681, which suggested that the educational level was the highest among riders occupying the nonmotor vehicle lane. Values of elasticity for educational level were all negative on the four intervals, the absolute value being about 0.070. On the one hand, this indicated that the educational level had low elasticity for the choice of illegal lane occupation behavior. That is, the educational level did not have a decisive role in the choice of illegal lane occupation behavior. On the other hand, it indicated that fewer riders chose to occupy motor vehicle lanes. This is because a rise in the riders' knowledge level boosted their safety awareness and traffic knowledge. More riders with a high educational level would voluntarily comply with traffic rules, and their behavior of illegal lane occupation decreased.

As shown in Table 10, the mean for driving age was 1.451, and no significant change in the mean was found on the four intervals. However, the mean on interval D was 1.515, which was slightly higher than that on the other three intervals. This indicated that the longer the driving age, the more likely the riders would occupy the motor lanes close to the middle isolation zone. This was because riders with a longer driving age were more proficient and skillful and more confident with riding. Therefore, these riders were more likely to occupy motor vehicle lanes closer to the middle isolation zone. The mean of elasticity for driving age on the four intervals was 0.364, which was smaller than 1.000. This indicated the lack of elasticity of driving age for the choice of illegal lane occupation behavior. Thus, driving age had little impact on the behavior of occupying motor vehicle lanes.

5.1.3. Temperament and Eye Vision. Table 11 shows the results on temperament and eye vision. According to the table, the mean for temperament increased steadily on the four intervals, the mean value being around 1.800. This indicated that the choice of illegal lane occupation behavior varied rather steadily with temperament. As indicated by the means, many of them were of a sanguine temperament. Values of elasticity for temperament on the four intervals were all more than 1.000, indicating high elasticity of temperament for the choice of illegal lane occupation behavior. The elasticity was the highest on interval B, the value being 1.656. This indicated that temperament had the greatest impact on the behavior of occupying the first motor vehicle lane. The specific relationship between temperament and behavior of illegal lane occupation is illustrated in Figure 4.

Figure 4 shows that among riders occupying motor vehicle lanes, those with sanguineous temperament accounted for the highest proportion. Moreover, the largest number of riders with such temperament occupied the nonmotor vehicle lane of all temperaments, followed by phlegmatic temperament. Similarly, as shown in Figure 4, the smallest number of riders with melancholic

Table 9: Calculation results for age and gender.

Interval for different lanes occupied	Selection probability	Gender			Age		
		Parameter value	Mean	Elasticity	Parameter value	Mean	Elasticity
A	0.287	0.491	0.835	0.292	0.730	1.022	0.532
B	0.124	0.491	0.910	0.391	0.730	1.085	0.693
C	0.289	0.491	0.878	0.306	0.730	0.878	0.456
D	0.300	0.491	0.879	0.302	0.730	1.061	0.542

Table 10: Calculation results on the educational level and driving age.

Interval for different lanes occupied	Selection probability	Educational level			Driving age		
		Parameter value	Mean	Elasticity	Parameter value	Mean	Elasticity
A	0.287	−0.059	1.681	−0.071	0.334	1.341	0.319
B	0.124	−0.059	1.616	−0.083	0.334	1.480	0.433
C	0.289	−0.059	1.633	−0.068	0.334	1.469	0.349
D	0.300	−0.059	1.545	−0.064	0.334	1.515	0.354

Table 11: Calculation results on temperament and eye vision.

Interval for different lanes occupied	Selection probability	Temperament (character)			Vision correction		
		Parameter value	Mean	Elasticity	Parameter value	Mean	Elasticity
A	0.287	1.030	1.637	1.203	0.430	0.209	0.064
B	0.124	1.030	1.836	1.656	0.430	0.186	0.070
C	0.289	1.030	2.122	1.554	0.430	0.184	0.056
D	0.300	1.030	1.879	1.355	0.430	0.152	0.046

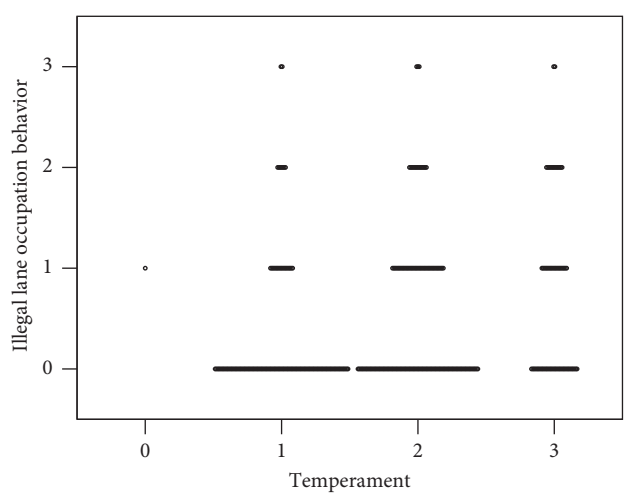

Figure 4: Relationship between temperament and illegal lane occupation behavior.

temperament chose such illegal behavior. Apparently, the number of riders with phlegmatic and sanguineous temperaments was the highest among all temperaments. Moreover, riders with sanguineous temperament were more likely to choose the behavior of illegal lane occupation. This indicated that riders with active, irritable, and extrovert personality were more likely to illegally occupy motor vehicle lanes.

During the process of e-bike riding, more than 80% of the information was collected by vision, and more than 90% of the information was dynamic. This relied heavily on the dynamic vision of the riders. The basis of dynamic vision is static vision, which lies at the root of cognition and judgment of the traffic environment. Corrected vision can meet the need for general information, but riders with corrected vision can still hardly have completely normal visual acuity. Moreover, the lens has a certain curvature, which causes mild deformation of the surrounding environment. This has a less significant impact on information acquisition when riding at a low speed in the motor vehicle lanes, but the impact can be considerable when riding at a high speed. As shown in Table 11, no significant difference in the mean for eye vision was observed on the four intervals, the value being about 0.183. This indicated that the riders' vision had no significant impact on the choice of illegal lane occupation behavior. Furthermore, riders with corrected vision accounted only for a small proportion of all e-bike riders. This further indicated that riders wearing eyeglasses still could not have completely normal eye vision for recognizing the surrounding environment. The values of elasticity for eye vision on the four intervals were 0.046–0.070, which were all smaller than 1.000. This indicated the lack of elasticity of eye vision for the choice of illegal lane occupation behavior. Thus, whether riders had corrected vision had little impact on the behavior of occupying motor vehicle lanes.

5.1.4. Occupation and Cycling Proficiency. Table 12 presents the results for occupation and cycling proficiency. According to the table, the mean for occupation was 1.482, and no significant difference in the mean was found on

Table 12: Calculation results on occupation and cycling proficiency.

Interval for different lanes occupied	Selection probability	Occupation			Cycling proficiency		
		Parameter	Mean	Elasticity	Parameter	Mean	Elasticity
A	0.287	0.417	1.253	0.372	1.919	2.033	2.782
B	0.124	0.417	1.559	0.569	1.919	2.311	3.883
C	0.289	0.417	1.510	0.448	1.919	2.531	3.453
D	0.300	0.417	1.606	0.469	1.919	2.182	2.932

intervals B, C, and D. The mean on interval A was 1.253, which was the smallest of all four intervals. This indicated that the number of students and employees was the highest of all riders illegally occupying motor vehicle lanes. In addition, they were more likely to occupy the nonmotor vehicle lane. Mean elasticity for occupation on the four intervals was 0.465, with all values of elasticity less than 1.000. This indicated that occupation had low elasticity on the choice of illegal lane occupation behavior. Therefore, the occupation had an insignificant impact on the choice of illegal lane occupation behavior.

Table 12 also shows that the mean for cycling proficiency increased steadily, the value being 2.264. This indicated that riders more skillful with riding were more likely to occupy the motor vehicle lanes. The reason is that as the driving age accumulates, the riders become more familiar with the road environment and infrastructure. Therefore, they are better prepared physiologically and physically when choosing to occupy the motor vehicle lanes. Values of elasticity for cycling proficiency on the four intervals were all more than 1.000, the value being 3.263. This indicated that cycling proficiency had high elasticity for the choice of illegal lane occupation behavior. This indicated that the higher the cycling proficiency, the higher the probability that the riders occupied the motor vehicle lanes. Moreover, values of elasticity were higher in intervals B and C, indicating that the cycling proficiency had the greatest impact on the choice of occupying the first (closer to the nonmotor vehicle lane) and second motor vehicle lanes. Relatively speaking, the probability that the riders occupied the third motor vehicle lane (closest to the middle isolation zone) was the smallest. The specific relationship between riding proficiency and behavior of illegal lane occupation is illustrated in Figure 5.

Figure 5 shows that the e-bike riders were more skillful with riding, and as the riding proficiency increased, an increasing number of riders occupied the motor vehicle lanes. This is because high riding proficiency is usually accompanied by richer driving age, better psychological quality, and higher demand for riding speed. For this reason, most of the e-bike riders would choose to occupy motor vehicle lanes with better road conditions. But when the riding proficiency reaches the highest, the number of violations decreases. This means experienced riders pay more attention to safety. In addition, the largest number of riders chose to occupy the nonmotor vehicle lane, to boost the traveling speed.

5.2. Correlation between Personal Characteristics, Traveling Speed, and Illegal Lane Occupation. Several different traffic groups use nonmotor vehicle lanes simultaneously, while the

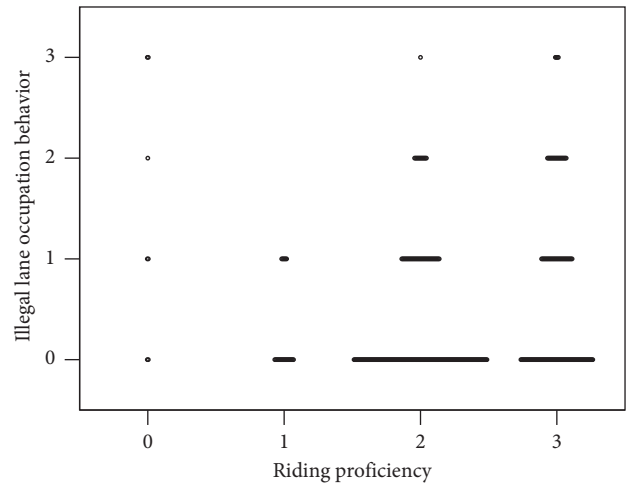

Figure 5: Relationship between riding proficiency and behavior of illegal lane occupation.

road infrastructure remains less developed compared with the motor vehicle lanes. Therefore, many e-bike riders prefer nonvehicle lanes for faster traveling or even overspeeding. Moreover, riders with different riding demand and riding habits occupy different positions of the motor vehicle lanes. In the present study, not only the influence of different personal characteristics of riders on the choice of traveling speed and illegal lane occupation behavior was analyzed but also the internal connections between the traveling speed of e-bike riders and the specific motor vehicle lane occupied were investigated.

e-bike riders prefer nonmotor vehicle lanes for the following reasons: the speed of the motor vehicle lane is much higher than the e-bike speed. There is a common sense that a slower one is easy to be hit by a faster one behind. So, the e-bike riders would not choose the motor vehicle lane to speed up, as that is obviously too dangerous. Although the nonmotor vehicle is narrow, pedestrians, bicycle, motorcycle, e-bike, and three-wheeler riders use the nonmotor vehicle lane simultaneously. It is safe than the motor vehicle lane. This directly results in lower traveling speed compared with the expectation on the part of e-bike riders. e-bikes need less space, which can basically meet the demand for traveling speed on the part of e-bike riders. Therefore, e-bike riders mostly prefer to occupy nonmotor vehicle lanes for faster movement. It can be inferred that illegal lane occupation correlates with overspeeding among e-bike riders, and such correlation is closely related to the personal characteristics of the riders. The specific relationship is shown in Figure 6.

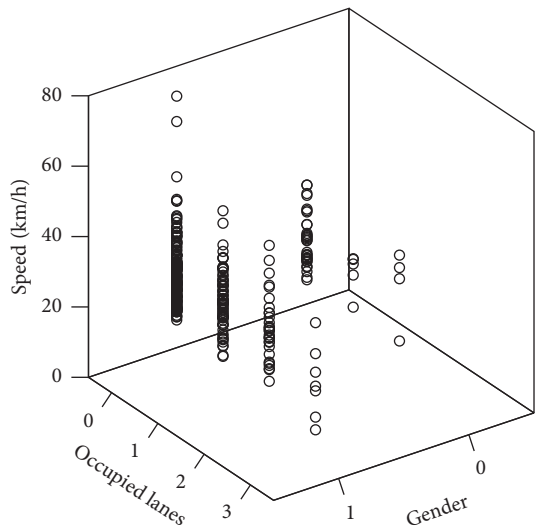

Figure 6: Relationship between traveling speed and illegal lane occupation behavior.

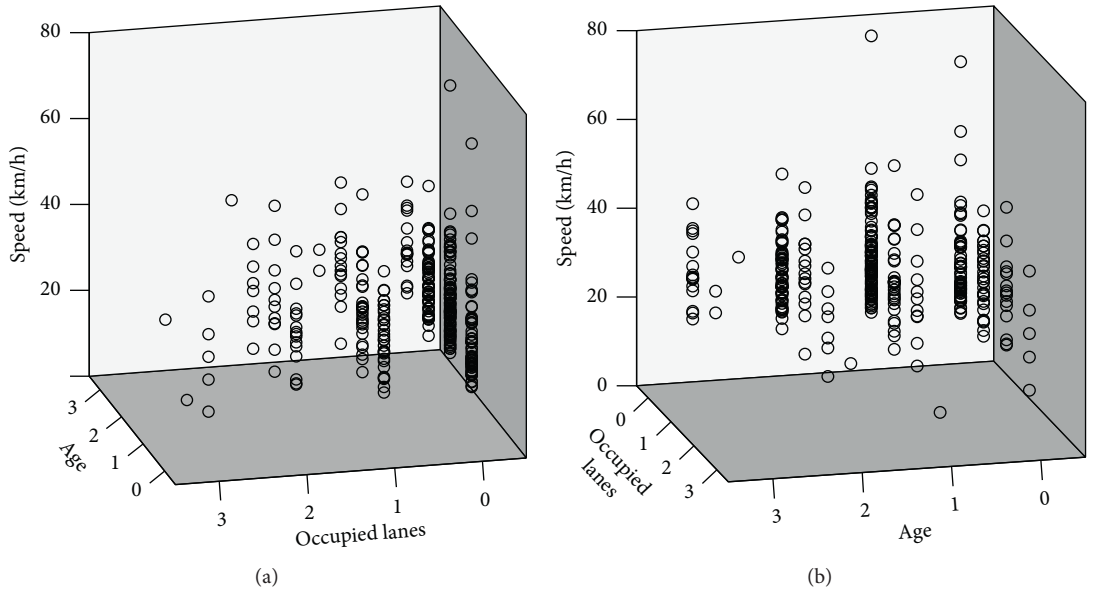

Figure 7: Relationship between age, traveling speed, and illegal lane occupation behavior.

Figure 6 shows that the majority of riders occupying the nonmotor vehicle lane were male, who traveled at the highest speed, which means overspeeding. It is easy to see that the largest number of male e-bike riders occupied the nonmotor vehicle lane for overspeeding.

Figure 7 shows that the age of riders occupying the nonmotor vehicle lane was about 30–45 years, and this age group also had the highest traveling speed. Riders aged between 30 and 45 years more frequently chose the behavior of illegal lane occupation, and the number of riders occupying the first motor vehicle lane was the highest.

Figure 8 shows that riders with junior and senior high school educational levels were more likely to occupy the nonmotor vehicle lanes and to overspeed. Riders with university and higher educational level were less likely to occupy the motor vehicle lanes. This indicated that the safety awareness and traffic knowledge level of riders with high educational level were higher compared with those with lower educational level.

Figure 9 shows that riders with a driving age of 1–3 below a year were more likely to occupy the motor vehicle lanes, and the traveling speed was the highest in riders occupying the nonmotor vehicle lane. This indicated that e-bike riders with fewer riding years were most likely to overspeed in the nonmotor vehicle lane.

Figure 10 shows that of the four types of temperament examined, those with sanguine and lymphatic temperaments were more likely to occupy the nonmotor vehicle lanes and

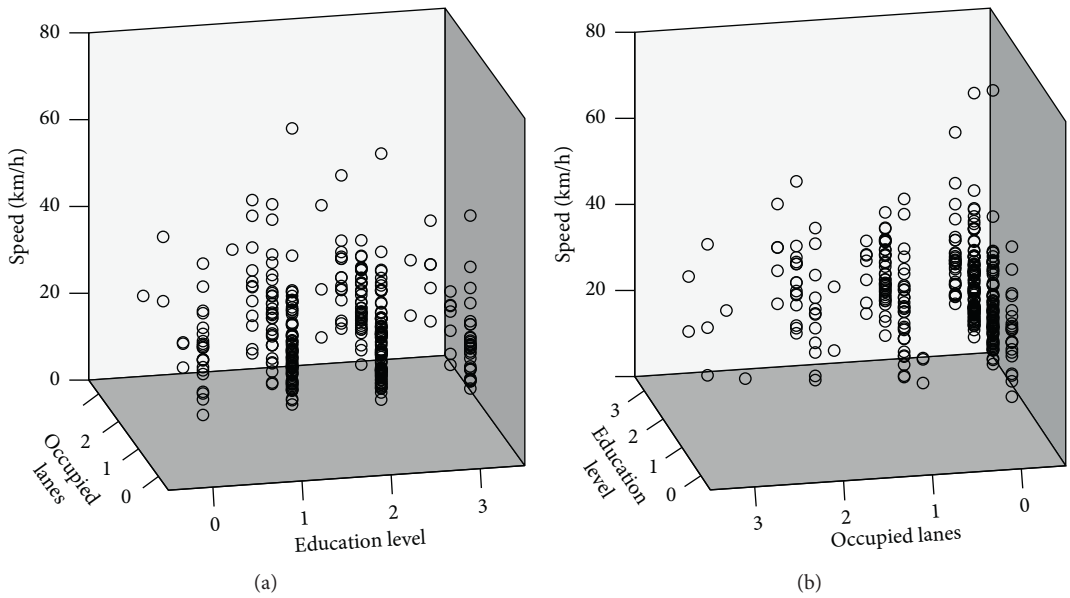

Figure 8: Relationship between the educational level, traveling speed, and illegal lane occupation behavior.

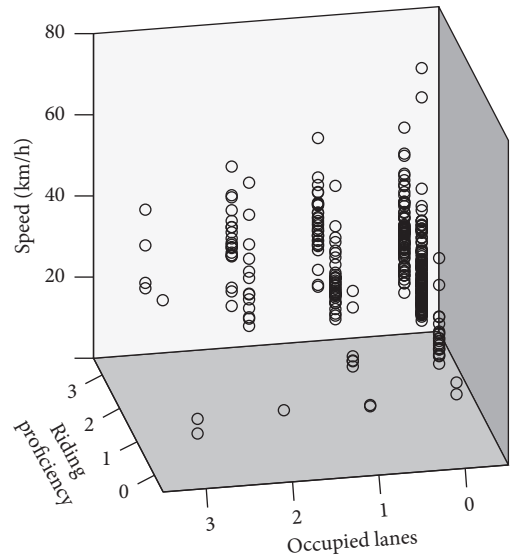

Figure 9: Relationship between driving age, traveling speed, and illegal lane occupation behavior.

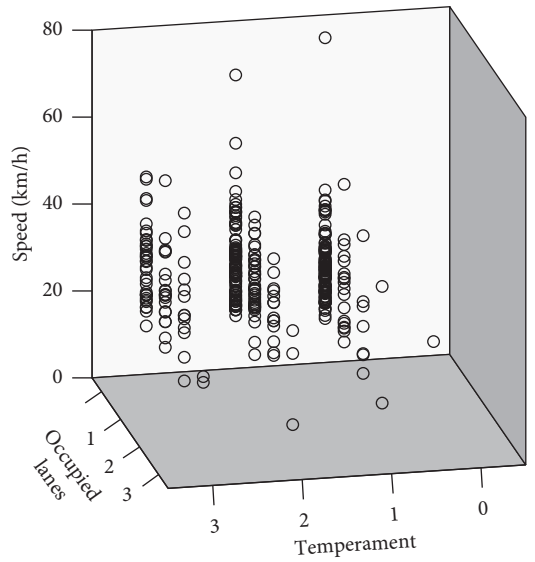

Figure 10: Relationship between temperament, traveling speed, and illegal lane occupation behavior.

to overspeed. The traveling speed of riders with lymphatic temperament occupying the nonmotor vehicle lane was the highest, exceeding 25 km/h, and the overspeeding behavior was most likely.

Figure 11 shows that it was most prevalent for employees to occupy motor vehicle lanes, and the employees occupying the nonmotor vehicle lane had the highest traveling speed. Relatively speaking, the traveling speed of retiree and students was lower. Very few students preferred traveling in the motor vehicle lanes, and their traveling speed was low. This was closely related to traffic safety awareness education and training at schools.

Figure 12 shows that the number of riders without corrected vision was the highest among all riders illegally occupying the motor vehicle lanes. Such riders were more likely to occupy the first motor vehicle lane and nonmotor vehicle lane and travel at the highest speed. As a result, illegal riding behaviors, such as overspeeding, were frequent.

Figure 13 shows that as the riding age increased and driving age became more abundant, e-bike riders were more likely to occupy the non- and first motor vehicle lanes. Moreover, the traveling speed of riders occupying the nonmotor vehicle lane was the highest, leading to the highest risk of illegal riding behaviors, such as overspeeding.

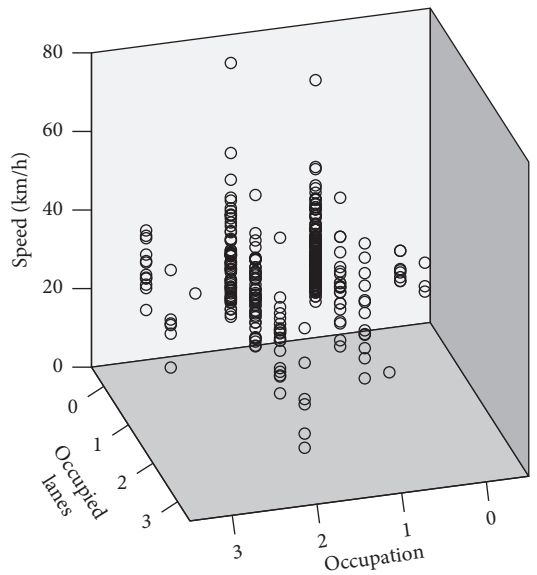

Figure 11: Relationship between occupation, traveling speed, and illegal lane occupation behavior.

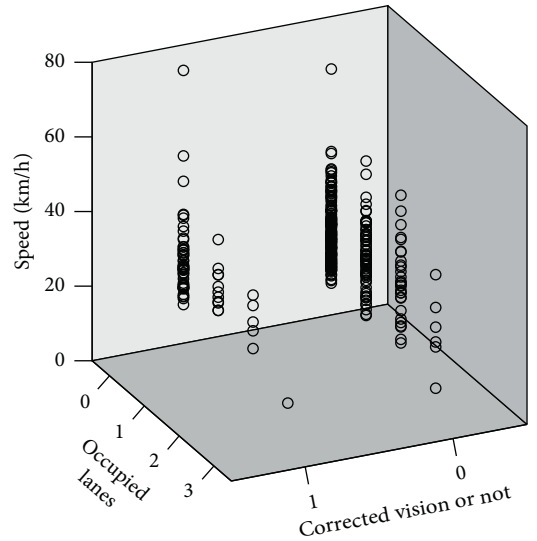

Figure 12: Relationship between eye vision, traveling speed, and illegal lane occupation behavior.

6. Conclusions and Future Study

6.1. Conclusions. Based on previous studies on traffic behaviors of e-bike riders, the influence of personal characteristics of e-bike riders and illegal lane occupation was further discussed. The specific personal characteristics influencing the choice of such illegal behavior were identified after measuring the correlation degrees. Moreover, concrete management strategies and schemes for safety education and skill training were proposed for e-bike riders with different personal characteristics. The ultimate purpose was to boost the traffic safety awareness of the riders and reduce risky riding behaviors and probability of traffic accidents. In this study, the temperament and cycling proficiency of riders significantly correlated with illegal riding behaviors. Therefore, effective regulatory measures should be formulated targeting these two aspects:

(1) The higher the riding proficiency of the e-bike riders, the higher the probability that the riders occupy the nonmotor vehicle lane, which poses a great threat to the riding safety. From another perspective, this highlights the importance of riding skills for ensuring safety. Therefore, traffic authorities should improve safety awareness and ethics for e-bike riders to ensure that every rider has enough skills and reduce inconvenience to pedestrians. Moreover, e-bike riders should wear protective equipment to minimize potential injury during riding.

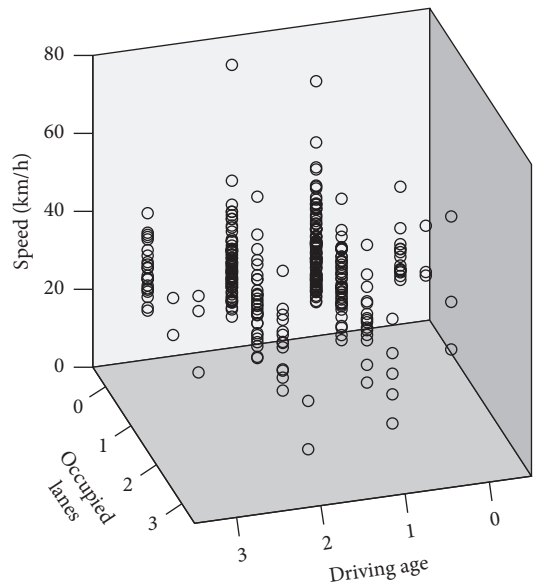

Figure 13: Relationship between driving age, traveling speed, and illegal lane occupation behavior.

(2) Traffic authorities should stop e-bike riders occupying nonmotor vehicle lanes on the road on a regular basis. These riders should be fined, and uniform safety education should be provided. In addition to safety precautions, these riders should be made to watch videos on traffic accidents of motor vehicles and those caused by illegal lane occupation to make them fully aware of the disadvantages of illegal lane occupation. Along with the safety education, webcast or road display should be used for notification on safety precautions for e-bike riders. While tightening law enforcement, all riders should be educated on the dangers of illegal lane occupation to boost safety awareness and safety riding behaviors.

(3) The root cause for illegal lane occupation is to achieve a faster speed. As indicated by the statistical analysis of sample data, it was found that the average traveling speed for riders occupying the second and third motor vehicle lanes was 25.1 km/h, which generally corresponded to overspeeding. Therefore, an illegal behavior warning device and a memory device should be installed on the e-bikes. These devices would transmit the riding data to traffic authorities in real time via the Internet. When e-bike riders overspeed in the nonmotor vehicle lane, voice prompts would remind the riders to travel at a safe speed. When e-bike riders overspeed in the nonmotor vehicle lane, not only voice prompts but also the rider information would be transmitted to the traffic authorities through the memory device. These riders would be singled out for safety education and penalty, so as to reduce the behaviors of illegal lane occupation and create a safe traffic environment.

In this study, first, the measurement model for assessing the influence of personal characteristics of electric vehicle riders on illegal lane behavior was built. The *t*-test was conducted indicating that the built model agreed well with the actual situation and had strong adaptability and practicability. Moreover, the model could quantify the degree of correlation between personal characteristics and illegal lane occupation. Second, elasticity theory was used to analyze the sensitivity of each influence factor to the choice of illegal lane occupation behavior. Finally, the influence of different personal characteristics of e-bike riders on risky riding behaviors was analyzed and the conclusions were drawn. The results showed that two personal characteristics, temperament and riding proficiency, had values of elasticity more than 1.000 for the choice of illegal lane occupation. In other words, these two influence factors were sensitive to the choice of illegal lane occupation behavior. Based on the riding speed obtained from the survey, the relationship between personal characteristics, traveling speed, and illegal lane occupation of e-bike riders was analyzed. As shown by analysis, riders with different personal characteristics traveled at different speeds on different lanes. The largest number of riders chose to travel in the first motor vehicle lane. The number of riders without corrected vision was also the highest among all riders occupying motor vehicle lanes. Riders with these characteristics were more likely to occupy the nonmotor vehicle lane and to overspeed.

6.2. Future Study. The sample values of this model had certain limitations, and the value range needs to be further expanded in future studies [48–51]. Moreover, other personal characteristics, such as marital status and body height, should also be included in the investigation. In addition, parameter values of each influence factor in the model need to be constantly modified so that the results of sensitivity

analysis are more accurate and better agree with the actual traveling situation.

The disaggregate model used in the present study had strong adaptability to individuals' traffic behaviors and the results obtained were reliable. In future studies, structural equation modeling should be used for stratification of the influencing factors. Observable variables described in this study need to be considered to study the relationship between potential variables and illegal lane occupation by e-bike riders.

Data Availability

The data used to support the findings of this study are available from the corresponding author upon request.

Conflicts of Interest

The authors declare that they have no conflicts of interest regarding the publication of this paper.

Acknowledgments

This research was funded by the National Natural Science Foundation of China (Project no. 71861023), the Program of Humanities and Social Science of the Education Ministry of China (no. 18YJC630118), the Natural Science Foundation of Zhejiang Province (no. LQ19E080003), the Natural Science Foundation of Ningbo Municipality (no. 2018A610127), the Philosophy and Social Science Program of Ningbo (G20-ZX37), and the Foundation of A Hundred Youth Talents Training Program of Lanzhou Jiaotong University.

References

[1] C. Ma, D. Yang, J. Zhou, Z. Feng, and Q. Yuan, "Risk riding behaviors of urban e-bikes: a literature review," *International Journal of Environmental Research and Public Health*, vol. 16, no. 13, pp. 2308–2322, 2019.

[2] E. Fishman and C. Cherry, "E-bikes in the mainstream: reviewing a decade of research," *Transport Reviews*, vol. 36, no. 1, pp. 72–91, 2016.

[3] Y. Guo, J. Zhou, Y. Wu, and J. Chen, "Evaluation of factors affecting e-bike involved crash and e-bike license plate use in China using a bivariate probit model," *Journal of Advanced Transportation*, vol. 2017, Article ID 2142659, 12 pages, 2017.

[4] Y. Guo, Z. Li, Y. Wu, and C. Xu, "Evaluating factors affecting electric bike users' registration of license plate in China using Bayesian approach," *Transportation Research Part F: Traffic Psychology and Behaviour*, vol. 59, pp. 212–221, 2018.

[5] China News Network, "China's electric bicycles have a social holding capacity of 250 million vehicles," 2017, http://news.ddc.net.cn/newsview_71477.html.

[6] Sohu.com, "The number of electric vehicles in nanning has exceeded 1.8 million," 2018, http://www.sohu.com/a/229498412_394146.

[7] Traffic Administration Bureau of the Ministry of Public Security, *People's republic of China Annual Report of Road Traffic Accidents (2016)*, Traffic Management Bureau of the Ministry of Public Security, Beijing, China, 2017.

[8] Y. Guo, Y. Wu, J. Lu, and J. Zhou, "Modeling the unobserved heterogeneity in e-bike collision severity using full Bayesian random parameters multinomial logit regression," *Sustainability*, vol. 11, no. 7, pp. 2071–2084, 2019.

[9] Traffic Management Bureau of Ministry of Public Security, *Statistics of Road Traffic Accidents in PRC (2015)*, Traffic Management Bureau of the Ministry of Public Security, Wuxi, China, 2016.

[10] F. Chen, S. Chen, and X. Ma, "Analysis of hourly crash likelihood using unbalanced panel data mixed logit model and real-time driving environmental big data," *Journal of Safety Research*, vol. 65, pp. 153–159, 2018.

[11] JSTV, "Nearly 70% of traffic accidents are related to electric bicycles," 2016, http://news.jstv.com/a/20160805/123632.shtml.

[12] W. Du, J. Yang, B. Powis et al., "Epidemiological profile of hospitalised injuries among electric bicycle riders admitted to a rural hospital in Suzhou: a cross-sectional study," *Injury Prevention*, vol. 20, no. 2, pp. 128–133, 2014.

[13] Compiled by national bureau of statistics of China," *China Statistical Yearbook*, China Statistics Press, Beijing, China, 2017.

[14] X. Ma, S. Chen, and F. Chen, "Multivariate space-time modeling of crash frequencies by injury severity levels," *Analytic Methods in Accident Research*, vol. 15, pp. 29–40, 2017.

[15] F. Hu, D. Lv, J. Zhu, and J. Fang, "Related risk factors for injury severity of e-bike and bicycle crashes in Hefei," *Traffic Injury Prevention*, vol. 15, no. 3, pp. 319–323, 2014.

[16] J. B. Zhou, Q. Y. Wang, M. J. Zhang, S. Dong, and S. C. Zhang, "An empirical study on seven factors influencing waiting endurance time of e-bike," *Journal of Transportation Systems Engineering and Information Technology*, vol. 17, no. 5, pp. 242–249, 2017.

[17] G. Ren, W. J. Wang, and Y. Zhang, *Traffic Behavior Safety of Non-motorized Traffic Participants-Modeling, Evaluation and Decision-Making System*, Science Press, Beijing, China, 2012.

[18] L. Yao and C. Wu, "Traffic safety for electric bike riders in China," *Transportation Research Record: Journal of the Transportation Research Board*, vol. 2314, no. 1, pp. 49–56, 2012.

[19] Y. Guo, P. Liu, L. Bai, C. Xu, and J. Chen, "Red light running behavior of electric bicycles at signalized intersections in China," *Transportation Research Record: Journal of the Transportation Research Board*, vol. 2468, no. 1, pp. 28–37, 2014.

[20] J. B. Zhou, Y. Y. Guo, W. U. Yao, and D. Sheng, "Assessing factors related to e-bike crash and e-bike license plate use," *Journal of Transportation Systems Engineering and Information Technology*, vol. 17, no. 3, pp. 229–234, 2017.

[21] C. X. Ma, J. B. Zhou, D. Yang, and Y. Y. Fan, "Research on the relationship between the individual characteristics of electric bike riders and illegal speeding behavior: a questionnaire-based study," *Sustainability*, vol. 12, no. 3, pp. 1–12, 2020.

[22] L. Steg and A. v. Brussel, "Accidents, aberrant behaviours, and speeding of young moped riders," *Transportation Research Part F: Traffic Psychology and Behaviour*, vol. 12, no. 6, pp. 503–511, 2009.

[23] M. A. Elliott, C. J. Baughan, and B. F. Sexton, "Errors and violations in relation to motorcyclists' crash risk," *Accident Analysis & Prevention*, vol. 29, no. 3, pp. 491–499, 2007.

[24] C. Q. Xie and P. Dianne, "A social psychological approach to driving violations in two Chinese cities," *Transportation Research Part F: Traffic Psychology and Behaviour*, vol. 5, no. 4, pp. 293–308, 2001.

[25] P. Ulleberg and T. Rundmo, "Personality, attitudes and risk perception as predictors of risky driving behaviour among young drivers," *Safety Science*, vol. 41, no. 5, pp. 427–443, 2003.

[26] C.-F. Chen, "Personality, safety attitudes and risky driving behaviors-evidence from young Taiwanese motorcyclists," *Accident Analysis & Prevention*, vol. 41, no. 5, pp. 963–968, 2009.

[27] J. P. Scheper, "The safety of electrically assisted bicycles compared to classic bicycles," *Accident Analysis & Prevention*, vol. 73, pp. 174–190, 2014.

[28] J. Reason, A. Manstead, S. Stradling, J. Baxter, and K. Campbell, "Errors and violations on the roads: a real distinction," *Ergonomics*, vol. 33, no. 10-11, pp. 1315–1332, 1990.

[29] G. Konstantina, "Modeling motorcycle helmet use in Iowa: evidence from six roadside observational surveys," *Accident Analysis & Prevention*, vol. 41, no. 3, pp. 479–484, 2009.

[30] L. T. Truong, H. T. T. Nguyen, and C. De Gruyter, "Mobile phone use among motorcyclists and electric bike riders: a case study of Hanoi, Vietnam," *Accident Analysis & Prevention*, vol. 91, pp. 208–215, 2016.

[31] M. Huan, X. Yang, and B. Jia, "Crossing reliability of electric bike riders at urban intersections," *Mathematical Problems in Engineering*, vol. 2013, Article ID 108636, 8 pages, 2013.

[32] W. Du, J. Yang, B. Powis et al., "Understanding on-road practices of electric bike riders: an observational study in a developed city of China," *Accident Analysis & Prevention*, vol. 59, pp. 319–326, 2013.

[33] M. Zhao, M. Yu, L. Fang et al., "Road-side observational survey on 4 unlawful acts among electric bicycle riders in Zhejiang," *Chinese Journal of Epidemiology*, vol. 37, no. 5, pp. 629–633, 2016.

[34] C. Wu, L. Yao, and K. Zhang, "The red-light running behavior of electric bike riders and cyclists at urban intersections in China: an observational study," *Accident Analysis & Prevention*, vol. 49, pp. 186–192, 2012.

[35] J. P. Schepers, E. Fishman, P. den Hertog, K. K. Wolt, and A. L. Schwab, "The safety of electrically assisted bicycles compared to classic bicycles," *Accident Analysis & Prevention*, vol. 73, pp. 174–180, 2014.

[36] T. Petzoldt, K. Schleinitz, S. Heilmann, and T. Gehlert, "Traffic conflicts and their contextual factors when riding conventional vs. electric bicycles," *Transportation Research Part F: Traffic Psychology and Behaviour*, vol. 46, pp. 477–490, 2017.

[37] M. Johnson and G. Rose, "Extending life on the bike: electric bike use by older Australians," *Journal of Transport & Health*, vol. 2, no. 2, pp. 276–283, 2015.

[38] C. R. Cherry, J. X. Weinert, and Y. Xinmiao, "Comparative environmental impacts of electric bikes in China," *Transportation Research Part D: Transport and Environment*, vol. 14, no. 5, pp. 281–290, 2009.

[39] X. Xing, W. Xu, Y. Chen, Z. Liu, Z. Bian, and Y. Liu, "A roadside observation study of unsafe riding acts among electric bicycle riders in a city of Anhui province," *Chinese Journal of Disease Control & Prevention*, vol. 21, pp. 943–946, 2017.

[40] H. Niu, X. Zhou, and X. Tian, "Coordinating assignment and routing decisions in transit vehicle schedules: a variable-splitting Lagrangian decomposition approach for solution symmetry breaking," *Transportation Research Part B: Methodological*, vol. 107, pp. 70–101, 2018.

[41] H. Niu, X. Zhou, and R. Gao, "Train scheduling for minimizing passenger waiting time with time-dependent demand and skip-stop patterns: nonlinear integer programming models with linear constraints," *Transportation Research Part B: Methodological*, vol. 76, pp. 117–135, 2015.

[42] F. Chen and S. Chen, "Injury severities of truck drivers in single- and multi-vehicle accidents on rural highways," *Accident Analysis & Prevention*, vol. 43, no. 5, pp. 1677–1688, 2011.

[43] Y. Guo, Z. Li, P. Liu, and Y. Wu, "Modeling correlation and heterogeneity in crash rates by collision types using full Bayesian random parameters multivariate Tobit model," *Accident Analysis & Prevention*, vol. 128, pp. 164–174, 2019.

[44] C. Ma, W. Hao, W. Xiang, and W. Yan, "The impact of aggressive driving behavior on driver-injury severity at highway-rail grade crossings accidents," *Journal of Advanced Transportation*, vol. 2018, pp. 1–10, 2018, 2018.

[45] GB17761-2018, "Electric bicycle safety technical specifications," *Electric Bicycle Safety Technical Specifications*, State Market Supervisory Administration/China National Standardization Administration, Beijing, China, 2018.

[46] S. Wu and F. M. Pan, *Statistical Analysis of SPSS*, Tsinghua University Press, Beijing, China, 2017.

[47] H. Niu, X. Tian, and X. Zhou, "Demand-driven train schedule synchronization for high-speed rail lines," *IEEE Transactions on Intelligent Transportation Systems*, vol. 16, no. 5, pp. 2642–2652, 2015.

[48] C. Ma, Changxi, R. He, and W. Zhang, "Path optimization of taxi carpooling," *PLoS One*, vol. 13, no. 8, Article ID e0203221, 2018.

[49] C. Ma, W. Hao, A. Wang, and H. Zhao, "Developing a coordinated signal control system for urban ring road under the vehicle-infrastructure connected environment," *IEEE Access*, vol. 6, pp. 52471–52478, 2018.

[50] C. Ma, "Network optimisation design of hazmat based on multi-objective genetic algorithm under the uncertain environment," *International Journal of Bio-Inspired Computation*, vol. 12, no. 4, pp. 236–244, 2018.

[51] C. Ma, W. Hao, F. Pan, and W. Xiang, "Road screening and distribution route multi-objective robust optimization for hazardous materials based on neural network and genetic algorithm," *PLoS One*, vol. 13, no. 6, Article ID e0198931, 2018.

Hindawi
Journal of Advanced Transportation
Volume 2020, Article ID 9689604, 14 pages
https://doi.org/10.1155/2020/9689604

Research Article

Multirotor Sizing Methodology with Flight Time Estimation

Marcin Biczyski,[1] **Rabia Sehab**,[1] **James F. Whidborne**,[2] **Guillaume Krebs**,[3] **and Patrick Luk**[4]

[1]*On-Board Energies and Systems Division, ESTACA Campus West, 53000 Laval, France*
[2]*Centre for Aeronautics, Cranfield University, MK43 0AL Cranfield, UK*
[3]*Pôle "Systèmes" ECo2, GeePs - CentraleSupelec, 91192 Gif sur Yvette, France*
[4]*Electric Power and Drives Group, Cranfield University, MK43 0AL Cranfield, UK*

Correspondence should be addressed to Marcin Biczyski; marcin.biczyski@estaca.fr

Received 26 July 2019; Accepted 15 October 2019; Published 20 January 2020

Guest Editor: Umberto Papa

This paper addresses the need for sizing of rotors for multirotor vehicle applications such as personal air transport, delivery, surveillance, and photography. A methodology for the propeller and motor selection is developed and augmented with flight time estimation capabilities. Being multirotor-specific it makes use of the platform's simplicity to rapidly provide a set of off-the-shelf components ready to be used in the vehicle. Use of operating points makes the comparison process fast, precise, and tailored to specific application. The method is easily implemented in software to provide an automated tool. Furthermore, clearly defined input and output parameters make it also usable as a module in other multicriteria optimisation algorithms. The new methodology is validated through comparison with a consumer-grade drone and the calculated results are compliant with manufacturer's specification in terms of maximum hover time.

1. Introduction

In recent years, Unmanned Aerial Vehicles (UAVs) have become a popular solution for a variety of civil and military applications including surveillance, photo- and videography, and land surveying. The versatility of these systems has even found them in many nonstandard purposes such as automated package delivery or Personal Air Vehicles (PAVs). Multirotor UAV platforms have gained particular attention due to their Vertical Take Off and Landing (VTOL) capabilities as well as their simple construction and control. Of paramount importance is safety and reliability, especially when it comes to autonomous solutions, and so the enterprise market offers complete, closed drone solutions at different size/weight points. These are simple-to-use systems with a high degree of user support and good performance for most applications. However, the mechanical simplicity of the platform means that customized and open solutions should be available for specialized applications. Furthermore, the main limitation of multirotor systems is their flight time, mostly due to battery weight and energy storage constraints. Therefore, a set of tools needs to be created that can aid the design of customized solutions that can be specifically tailored for a particular application. Thus there is a need for a methodology to automatically select the best consumer-grade components to build a custom solution at a given weight and performance level.

There are some methodologies in the open literature for this purpose, but few lead directly to a "bill-of-materials" level solution. The most popular approach to obtaining a "flyable" configuration seems to be to test various *motor + propeller* combinations and choose one that suits the application [1]. Although popular with hobbyists, the method has little value in the commercial or research environment due to high cost (purchase of components), time requirement, and the need for specialized equipment (thrust stand, dynamometer). This method provides the most accurate results, but the number of combinations needed to be tested increases geometrically with each added component. This process can be significantly sped up using calculators such as Drive Calculator [2] and eCalc [3], which incorporate some of the data in their databases, but still the selection needs to be performed manually. This lack of search automatization capability and weak interfacing with other software (e.g., MATLAB) renders it difficult when analysing more than one case. In addition, eCalc does not pay that much attention to the main lifting body – the propeller, and uses a mathematical model (diameter and pitch can be input manually) for the performance calculation, as opposed to a more accurate database of measured/simulated data. Therefore,

alternative methods can still be proposed that improve accuracy, versatility or usability of database-driven approach.

Multirotor-specific methodologies have been developed by Gatti and Giulietti [4], Gatti [5] and Kim et al. [6]. They all used statistical methods to estimate relations between different components of the propulsion chain. The first two use analytical methods from the area of aerospace to calculate take-off weight based on mission requirements, and the last manages to simplify the drone propulsion model to a single equation to obtain generated power or thrust. Unfortunately, these approaches provide too little data to properly size the components, and in some cases even require the data of a selected component to work. Therefore, while useful for calculating the target multirotor weight for the application, they cannot be used for the component selection process.

Although not solving the problem completely, there are several methods that help with the preliminary multirotor design. Basset et al. [7] present past and current efforts to develop UAV presizing methodologies. They focus on conceptual, as well as numerical aspects of the vehicle. Due to the confidential nature of the projects, the paper does not go into much detail of the inner workings of the methodologies. However, most of them share a trait of being as general as possible in order to make them applicable to every configuration, which is not desired when dealing with an already chosen topology, such as multirotor, due to possible oversimplification and loss of optimisation opportunities.

A detailed database-free multirotor sizing methodology has been presented by Bershadsky et al. [8], that has been implemented in a tool called Electric Multirotor Sizing Tool (EMST). The authors have shown its versatility and accuracy with several examples. Unfortunately, their parametric approach requires heavy generalisation of component models, that keeps the mean error low, but may lead to significant errors for more unusual configurations. Yet, the authors have demonstrated award-winning results even for very tight constraints. However, it should still be possible to achieve a similar level of accuracy with alternative methods, with the added benefits of reduced computational cost and increased flexibility through decreased number of dependencies in the system.

Dai et al. [9] have addressed a very important issue, that is often neglected in other texts – the selection of components that best match calculated parameters. The proposed methodology divides the sizing problem into twelve sub-problems: eight of them optimise weight and efficiency of the components and the remainder four try to best match a real component to the calculated optimised parameters. Unfortunately, this degree of compartmentalization has the disadvantage that the real product parameters do not affect the optimisation process and this restricts the opportunity for further improvement of the design. It is especially important, as in a more recent paper [10] the authors focus on the role of propeller optimisation and the importance of propeller and motor coupling.

A different approach was taken by Magnussen et al. [11] who treated the propulsion system sizing problem as a mixed-integer programming problem. The strengths of this method are a solid definition of the base problem and the ability to use external solvers. However, the user still needs to provide the data of considered components. The added value of this methodology is the ability to model the dynamic motor thrust response, which is a useful tool for dynamic performance analysis. However, for basic sizing applications the complexity (up to 3091 variables in the example problem) may be too overwhelming and a simpler solution may be preferred.

Figure 1: Multirotor in *quad X* configuration with visible components of the propulsion chain. (i) Flight Controller, (ii) ESC (under arm), (iii) BLDC Motor, (iv) propeller, and (v) battery connector.

This paper presents a method for sizing of the multirotor propulsion system through the selection of propeller and motor. Furthermore, the method provides the necessary data for the selection of the Electronic Speed Controller (ESC) and battery. Additionally, it gives a way of comparing different configurations through estimation of flight time by modelling battery discharge at constant power requirement. The key point of the methodology is the fact that it works on real components (propellers and motors) increasing the precision of the estimation. Another feature is the ability for the selection process to be automated making it an useful module for use in novel optimisation algorithms. Elements of optimisation are included in order to provide efficient and feasible solution. However, it should be noted that the resultant configuration is based on estimations, assumptions and inaccurate data, and therefore not optimal, so the methodology results should be treated only as a *good first guess*.

The paper is structured as follows; Section 2 details all the elements of the multirotor propulsion chain and their interaction; Section 3 describes the methodology based on the inverted model from the previous section; Section 4 presents example results for a small drone such as DJI Phantom 4 V2.0 and extends the findings onto Personal Air Vehicles; finally, Section 5 concludes the paper and highlights the most important outcomes.

2. Multirotor Propulsion Chain

Multirotors as a category of flying vehicles cover a lot of variants differing not only in the number of rotors, but also their placement. Currently, the most popular configuration

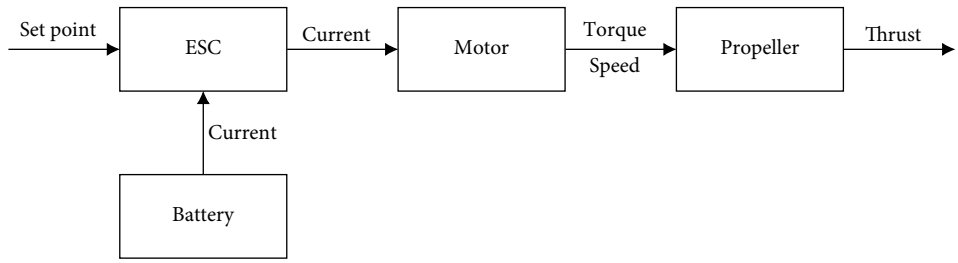

Figure 2: Multirotor propulsion chain diagram.

seems to be *quad X* with four parallel rotors placed diagonally from the center, as shown in Figure 1. One of the characteristic properties of most multirotors is their symmetry and the fact that every arm is the same, except for the rotor spinning direction. This makes it easy to analyse the propulsion system for the general case by analysing only one arm (one propulsion chain). The Flight Controller (FC) is responsible for control strategy for the whole platform and preparing a set point for each arm, but it does not participate in the propulsion chain as such.

In most cases, Brushless DC (BLDC) motors are used for multirotor propulsion, but sometimes, usually for toys under 100 g, DC motors are also used. This paper focuses only on BLDC; however, most concepts shown apply to both types. Brushless motors do not have physical brushes, so they require Electronic Speed Controllers (ESC) to achieve electronic commutation. Therefore, the main components of the propulsion chain are identified to be: *propeller*, *motor*, *ESC,* and *battery*. A schematic of the propulsion model of a multirotor is shown in Figure 2. It can be seen that there is one input of a set point (given by FC) and one output, namely the thrust generated by the propeller. Therefore, the propulsion chain can be identified as a open-loop Single Input Single Output (SISO) system, which makes it relatively easy to size components one at a time. In the next part of this section, each component will be described in detail.

2.1. Propeller. Aircraft propellers are characterized by 3 main parameters: diameter, pitch, and the number of blades. Generally, the higher these are, the higher the thrust generated, but also higher torque is exerted on the motor. However, long, slowly spinning, 2-bladed propellers are known to be more aerodynamically efficient than small, fast-spinning, multibladed ones. Propeller characteristics are mainly a function of its rotational speed and the speed of incoming air. However, if we consider air density to be constant and the air to be static (at hover in still air), the thrust, torque, and power depend only on propeller speed. Additionally, there are secondary parameters such as mass and geometry template expressed as manufacturing series (e.g., Multirotor, Slow Flyer, Carbon, etc.).

2.2. Motor. In a multirotor, the motor's main objective is to drive the propeller reliably and with high acceleration, so the speed can be changed quickly. The main limitations of a BLDC motor are in terms of speed and current. Maximum current is often stated by the manufacturer and maximum speed in no-load conditions ω_0 can be calculated from the KV parameter multiplied by the applied voltage V:

$$\omega_0 = \mathrm{KV} \times V. \tag{1}$$

With a constant voltage, when current is applied, the motor starts exerting torque on the shaft accelerating it until its torque equals the load torque, assuming the mechanical losses are neglected. At low speed, far from the motor constraints, it is assumed that the relation between motor torque and current is constant and expressed with motor torque constant (K_T). Therefore, the applied current is transformed into the torque based on the motor characteristic, then the torque is transformed into speed based on the propeller torque–speed characteristic, and finally the speed is transformed into thrust using the propeller thrust–speed characteristic. This sequence makes the propulsion chain easy to calculate analytically as a SISO system.

2.3. Electronic Speed Controller. Although Electronic Speed Controllers (ESCs) serve a very important purpose in the real-life multirotor, in the propulsion chain model it has very little importance. In the model, its function is reduced to transferring current from the battery to the motor under constant voltage. However, when designing a multirotor, ESC still needs to be sized according to the maximum current flowing to the motor.

2.4. Battery. When it comes to lightweight aerial vehicles, Lithium Polymer (LiPo) batteries currently dominate the market due to their high energy density and high current discharge capabilities [5, 12]. These batteries are composed of several cells connected in series (rarely in parallel). Cell voltage changes according to the state of charge with 4.2 V being at 100%, 3.85 V at 50% and 3.7 V (nominal) at 20%. However, discharging a LiPo cell under 3 V leads to permanent damage to the battery. Therefore, it is recommended to only discharge the batteries to about 20%, which grants a Depth of Discharge (DoD) of 80%. The cells can be connected in series or in parallel, denoted by *S* or *P,* respectively, so for example, 4*S*1*P* is a 4 cell battery with 14.8 V nominal voltage. Additionally, the batteries are characterized by their capacity in mAh and a C-rating (r_C), which specifies the maximum current that can be drawn continuously, for example 35 C × 5.2 Ah = 182 A (the unit being C and not Coulomb). It is evident that maximum discharge current is not dependent on battery capacity.

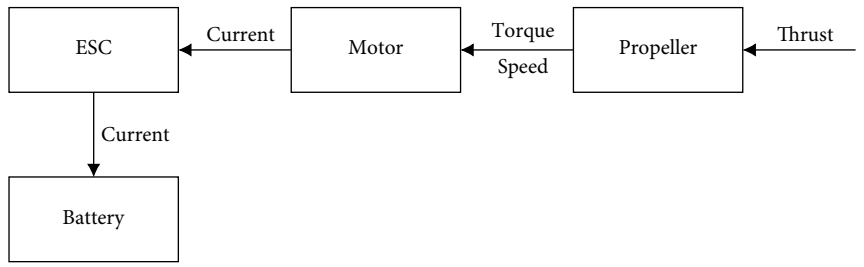

Figure 3: Inverted multirotor propulsion chain diagram.

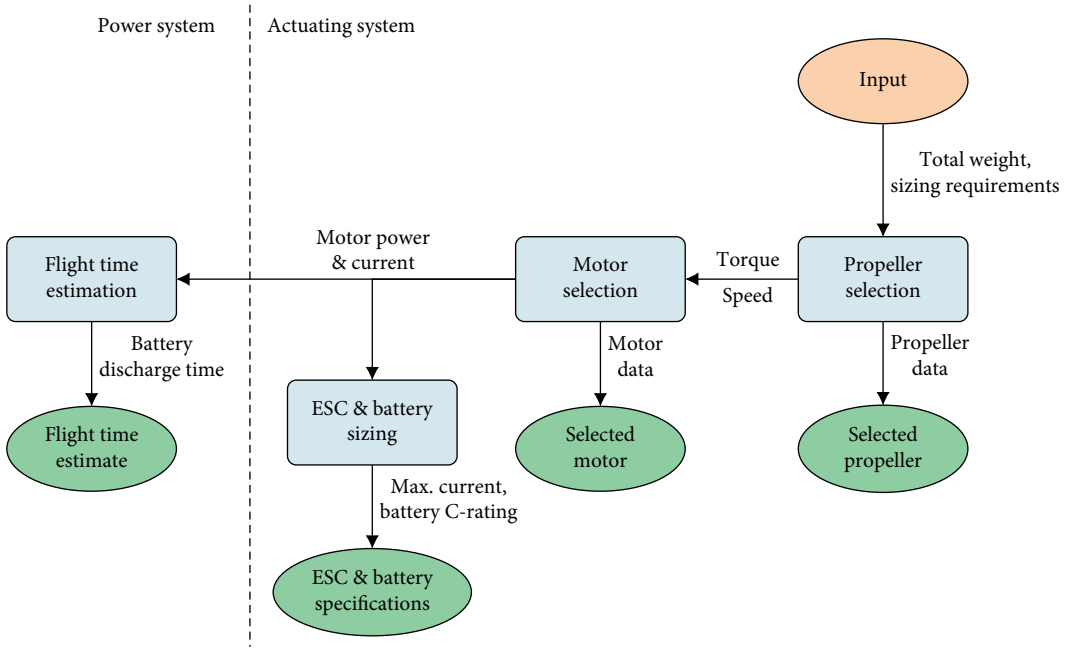

Figure 4: Simplified sizing methodology flowchart with division into two sub-systems.

3. Sizing Methodology

By inverting the propulsion system model developed in the previous section, a new model can be obtained allowing to estimate battery voltage based on thrust generated, as shown in Figure 3. This allows for an iterative approach in order to determine the time required to deplete the battery at constant power draw, which effectively serves as a flight time estimate. Thus, two distinct subsystems can be distinguished in the system model: the actuating system and the power system. This manifests itself in the sizing methodology, which is also divided into two parts. Figure 4 shows a simplified view of the methodology. Although it is based on the diagram in Figure 3, it also shows the separation between battery sizing and battery simulation (flight time simulation).

3.1. Actuating System. The actuating system provides the thrust propulsion to the vehicle and consists of the propeller, the motor, an ESC to control the motor and a battery to power the motor. The propeller sizing and selection is performed first, the motor sizing being dependent on the propeller properties. Finally, specifications for the ESC and the battery are produced.

The propulsion system model used here is only applicable in static conditions and at constant speed. Modelling a multirotor in flight is much more complicated due to the presence of aerodynamic effects such as variable angle of attack, reduction of thrust coefficient with advance ratio, and additional frame drag. However, an approximation of the required performance for full controllability in flight is made using the model only in static conditions of operation. It uses a state of equilibrium achieved at hover (in no-wind conditions), where thrust generated by the propellers is equal to the multirotor's weight. This thrust can be multiplied by a constant thrust-to-weight ratio to achieve a value of static thrust that guarantees specific performance in the air depending on the application. This approach appears imprecise; however, during the years of use of similar methods in the community of radio controlled aircraft modellers, the values of thrust-to-weight ratio required for different applications have been validated with many test flights. A quick summary of typical values can be found in Table 1, which is based on [13, 14]. Additionally, in static conditions there is no influence of rotor inertia on motor performance, so the propeller and motor selection can be decoupled, further simplifying the process.

Table 1: Typical applications for multirotors of different thrust-to-weight ratios.

Thrust-to-weight ratio	Application
2	Slow flight (minimum)
3	Payload transport; photography
4	Surveillance
5+	Aerobatics; high-speed video
7+	Racing

3.1.1. Propeller Sizing and Selection. The propeller sizing and selection process starts by defining a propeller database represented as a set of available propellers

$$\mathscr{P} := \{\mathbf{p}_i : i = 1, \ldots, n_p\}, \tag{2}$$

where the ith propeller $\mathbf{p}_i$ is defined by the pair

$$\mathbf{p}_i := (\mathbf{f}_{pi}, g_{pi}), \tag{3}$$

where $\mathbf{f}_{pi}$ denotes the ith propeller performance, which will be defined later, and g_{pi} denotes its physical properties expressed as a 4-tuple

$$g_{pi} := (d_i, \theta_{pi}, m_{pi}, s_{ni}), \tag{4}$$

where d_i is the ith propeller diameter, θ_{pi} is its pitch angle, m_{pi} is its mass, and s_{ni} is a discrete parameter representing the propeller series name. The propeller set $\mathscr{P}$ is then filtered to obtain a set of propellers $\mathscr{P}_p \subseteq \mathscr{P}$ that satisfy a requirement 4-tuple

$$g_{pr} = (d_{\min}, d_{\max}, m_{p_{\max}}, \mathscr{S}_{nr}), \tag{5}$$

where $d_{\min}$ is the minimum diameter, $d_{\max}$ is the maximum diameter, $m_{p_{\max}}$ is the maximum mass, and $\mathscr{S}_{nr}$ is a set of preferred series names

$$\mathscr{S}_{nr} := \{s_{nk} : k = 1, \ldots, n_s\}. \tag{6}$$

Thus

$$\mathscr{P}_p = \{\mathbf{p}_i : d_i \in [d_{\min}, d_{\max}], m_{pi} \in (0, m_{p_{\max}}], s_{ni} \in \mathscr{S}_{nr}\} \tag{7}$$

This helps save time when evaluating the performance data and calculating operating points that is done next.

The performance of the ith propeller $\mathbf{f}_{pi}$ is denoted as a triplet of bijective mappings

$$\mathbf{f}_{pi} := (\omega \mapsto T(\omega), \omega \mapsto \tau(\omega), \omega \mapsto P_p(\omega)), \tag{8}$$

where ω is the rotor speed, T is the thrust, τ is the torque, and P_p is the propeller power. Let $T_r^{(k)}$ denote a required thrust. For each $\mathbf{p}_i \in \mathscr{P}_p$, we determine a set of n_o operating points $o_{pi} = \{o_{pi}^{(k)} : k = 1, \ldots, n_o\}$ where

$$o_{pi}^{(k)} := (T_i^{(k)}, \omega_i^{(k)}, \tau_i^{(k)}, P_{pi}^{(k)}) \tag{9}$$

and where

$$T_i^{(k)} = T_r^{(k)}, \tag{10}$$

$$\omega_i^{(k)} = T^{-1}(T_r^{(k)}), \tag{11}$$

$$\tau_i^{(k)} = \tau(\omega_i^{(k)}), \tag{12}$$

$$P_{pi}^{(k)} = P_p(\omega_i^{(k)}). \tag{13}$$

An example of the mapping triplets for two propellers is shown in Figure 5 along with an illustration of obtaining o_{pi} from T_r.

Usually $n_o = 2$ operating points are calculated: the operating point at hover $o_{pi}^{(1)}$, and the Wide Open Throttle (WOT) operating point $o_{pi}^{(2)}$. These signify the lower and upper boundaries of the flight performance, respectively. A third operating point ($k = 3$) can also be defined that corresponds to the propeller limit speed designated by the manufacturer; this can be used for checking the feasibility of the other operating points. The thrust requirements, $T_r^{(1)}$ for the hover condition and $T_r^{(2)}$ for the WOT condition, can be calculated from

$$T_r^{(1)} = \frac{W_{\text{total}}}{n_{\text{rot}}}, \tag{14}$$

$$T_r^{(2)} = r_T \times T_r^{(1)}, \tag{15}$$

where W_{total} is the estimated total weight of the multirotor, n_{rot} is the number of rotors and r_T is the thrust-to-weight ratio. Except for the propeller (and motor) set filtering purposes, the methodology uses only the total estimated weight of the multirotor, as it is presumed that the frame, battery size, payload and control modules are preselected from the ones available to the user and suited for the application. As only static conditions are considered (multirotor inertia not considered), the weights of those components are of lower importance as opposed to the estimated weights of propellers, motors and ESCs, which are multiplied by the number of rotors

$$\begin{aligned} W_{\text{total}} = {} & n_{\text{rot}}(W_{\text{prop}} + W_{\text{motor}} + W_{\text{ESC}}) \\ & + W_{\text{frame}} + W_{\text{battery}} + W_{\text{payload}} + W_{\text{FC}} + W_{\text{other}}. \end{aligned} \tag{16}$$

In practice, due to the fact that the propeller characteristics mappings defined by (8) are often given in the form of sample points, interpolation must be used for the calculations. This introduces errors. Therefore, although in theory $P_p = \tau\omega$, often in practice (dependence on k removed for notational simplicity)

$$P_{pi} \neq \tau_i \omega_i, \tag{17}$$

hence an average of those two values is taken

$$P_{pi_{\text{avg}}} = \frac{1}{2}(P_{pi} + \tau_i \omega_i). \tag{18}$$

To choose the propeller, various selection criteria are available. If $n_o > 1$, then determining the minimum power solution is a

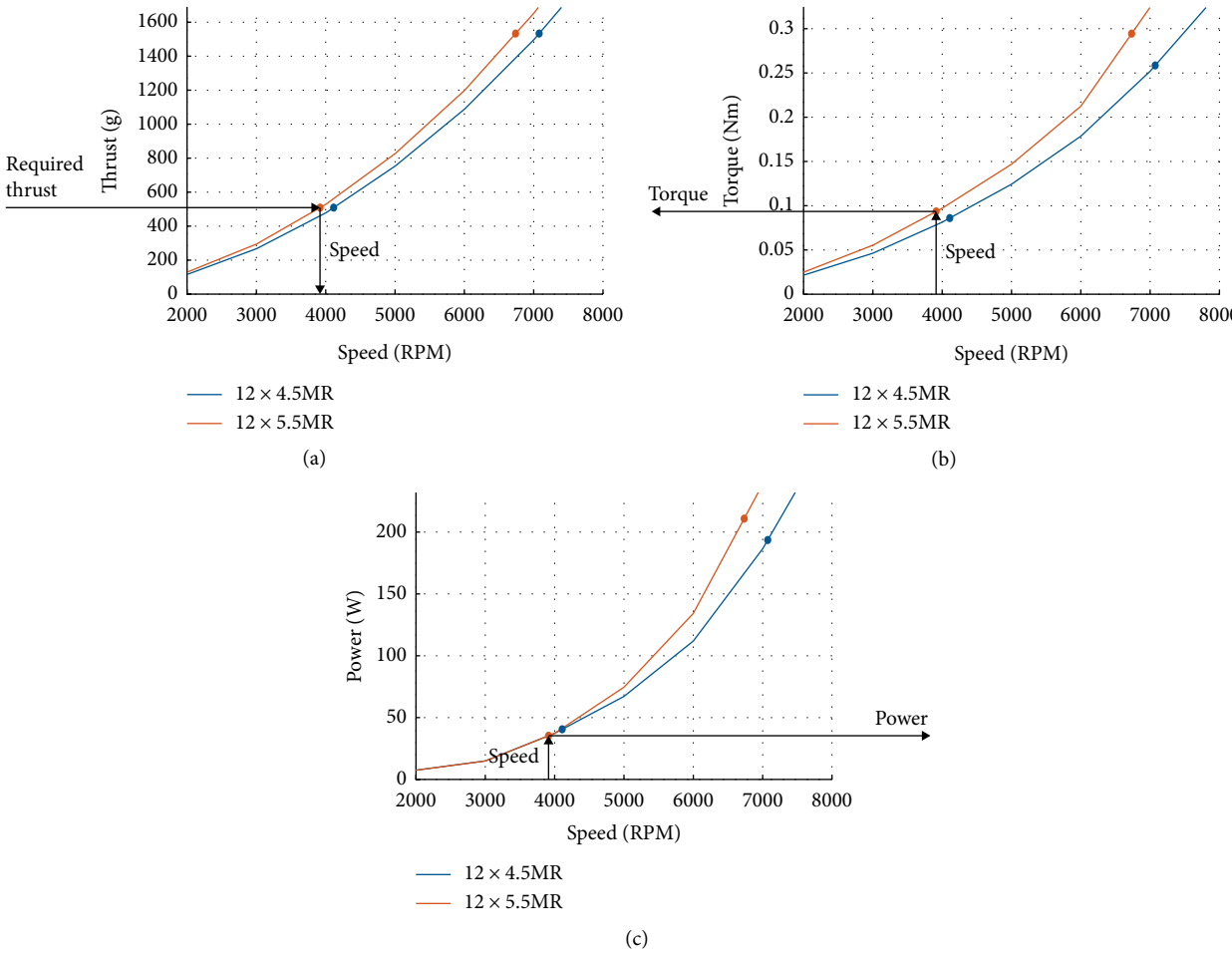

FIGURE 5: Example of obtaining a propeller operating point based on required thrust. (a) Obtaining speed from required thrust. (b) Obtaining torque from speed calculated in (a). (c) Obtaining power from speed calculated in (a).

multiobjective problem, and some user interaction is then helpful in making the selection. However, it is often possible to reduce the problem to the simplest case for $n_o = 1$, where the lowest power at hover operating point can be computed as follows

$$\mathbf{p}_{\text{selected}} := \arg\min_{\mathbf{p}_i \in \mathscr{P}_p} P^{(1)}_{pi_{\text{avg}}}. \tag{19}$$

In this case, the minimization can be quickly carried out through exhaustive search, thanks to the small set size due to the filtering in previous steps.

3.1.2. Motor Sizing and Selection. In a similar manner as for the propeller, let $\mathscr{M}$ be the set of available motors

$$\mathscr{M} := \left\{\mathbf{m}_j = \left(\mathbf{f}_{mj}, g_{mj}\right) : j = 1, \ldots, n_m\right\}, \tag{20}$$

where $\mathbf{f}_{mj}$ is the motor model described by the triplet of mappings

$$\mathbf{f}_{mj} := \left(I \mapsto P_m(I), I \mapsto P_e(I), \left(P_m, P_e\right) \mapsto \eta\left(P_m, P_e\right)\right), \tag{21}$$

where I is the current, P_m is the mechanical power, P_e is the electrical power, η is the efficiency and where g_{mj} denotes the motor properties expressed as a triplet

$$g_{mj} := \left(I_{\max_j}, \omega_{0j}, m_{mj}\right), \tag{22}$$

where $I_{\max_j}$ is the maximum allowable ith motor current, ω_{0j} is its maximum no-load speed and m_m is its mass.

Unlike the process for the propeller selection, the performances of the motors must be evaluated first. The required motor power is set to be $P_r = P^{(k)}_{p_{\text{selected}}}$. Then for each $\mathbf{m}_j \in \mathscr{M}$, we determine n_o motor operating point triplets

$$o^{(k)}_{mj} := \left(I^{(k)}_j, P^{(k)}_{ej}, \eta^{(k)}_j\right), \tag{23}$$

where (dependence on k removed for simplicity)

$$I_j = P_m^{-1}(P_r), \tag{24}$$

$$P_{ej} = P_e\left(I_j\right), \tag{25}$$

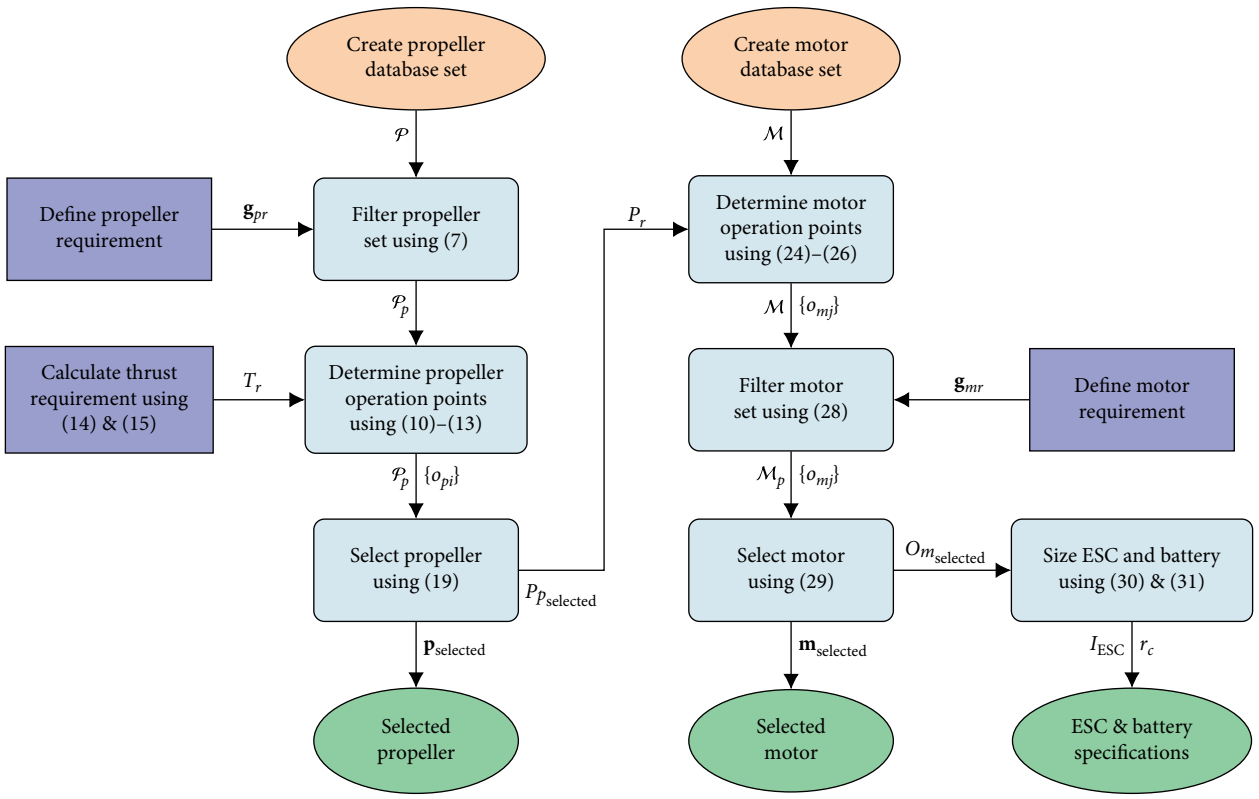

Figure 6: Actuating system sizing methodology information flow diagram.

$$\eta_j = \eta\left(P_r, P_{ej}\right). \tag{26}$$

It should be noted that the mapping $I \mapsto P_m(I)$ is not bijective in terms of motor characteristics, because at high current values most of the energy is dissipated as heat. However, considering the domain only up to the maximum current specified by manufacturer, the function is almost always monotonic. Therefore, in practice, over the domain $\left[0; I_{\max_j}\right]$ the inverse of power function P_m^{-1} can almost always be evaluated.

Knowledge of o_{mj} for all $\mathbf{m}_j \in \mathscr{M}$ allows for filtering of the motor set in regards to maximum current, speed and mass, thus obtaining $\mathscr{M}_p \subseteq \mathscr{M}$ that satisfies maximum current requirement on each motor $I_j \leq I_{\max_j}$ and a requirement pair

$$g_{mr} = \left(\omega_{\max}, m_{m_{\max}}\right), \tag{27}$$

where $\omega_{\max} = \omega^{(2)}_{\text{selected}}$ is the propeller speed at WOT and $m_{m_{\max}}$ is the maximum motor mass. Thus

$$\mathscr{M}_p = \left\{\mathbf{m}_j : I_j \leq I_{\max_j}, \omega_{0j} \geq \omega_{\max}, m_{mj} \leq m_{m_{\max}}\right\}. \tag{28}$$

Like in the propeller's case, various selection criteria could be used to choose the motor. In the simple example for $n_o = 1$ it could be the lowest electrical power

$$m_{\text{selected}} := \arg \min_{\mathbf{m}_j \in \mathscr{M}_p} P^{(1)}_{ej}. \tag{29}$$

Table 2: Data contained in sizing methodology outputs.

Output name	Data contained
Propeller specification	Name; diameter d; pitch θ_p; series s_n
Motor specification	Name; KV rating; rated speed $\omega^{(2)}_{\text{selected}}$; rated torque $\tau^{(2)}_{\text{selected}}$; rated mech. power $P^{(2)}_{m_{\text{selected}}}$; rated el. power $P^{(2)}_{e_{\text{selected}}}$; rated efficiency $\eta^{(2)}_{\text{selected}}$; nominal voltage V
ESC specification	Maximum current I_{ESC}
Battery specification	Cell number n_C; minimum C-rating r_C; capacity C

Again the filtering operation in (28) makes it possible to use exhaustive search for the minimization purpose.

3.1.3. ESC and Battery Sizing. The Electronic Speed Controller is sized mainly in regards to the maximum current it can handle. As it is assumed that the multirotor will never need more thrust than achieved at WOT operating point, the current should also not go over the calculated value. Therefore, it can be said that

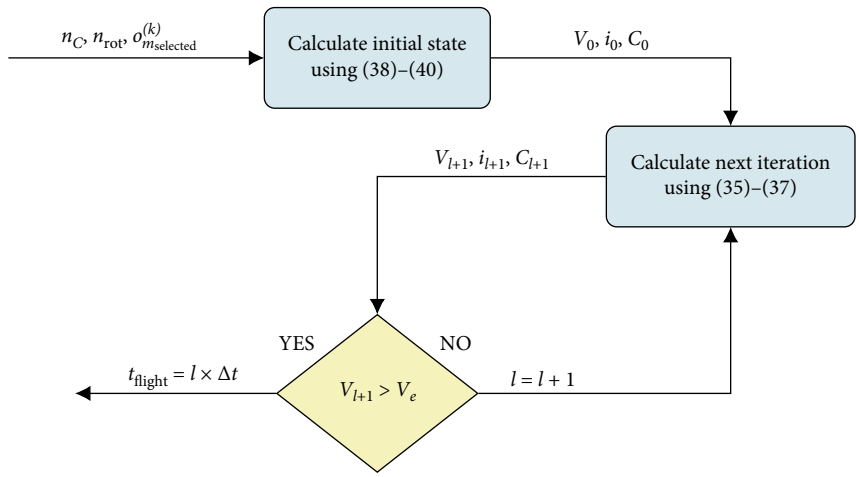

Figure 7: Power system calculation flowchart for kth operating point.

$$I_{ESC} = I^{(2)}_{selected}, \tag{30}$$

where I_{ESC} is the rated (maximal) ESC current and $I^{(2)}_{selected}$ is the motor current at WOT operating point.

A substantial part of battery specification needs to be provided by the user to realise flight time estimation as described in Section 3.2. However, the methodology allows to complete the battery specification by sizing the C-rating parameter

$$r_C = \frac{I_{ESC} \times n_{rot}}{C}, \tag{31}$$

where r_C is the minimal required battery C-rating and C is the battery capacity.

The whole actuating system sizing methodology is depicted by the data flow chart shown in Figure 6. It shows the dependence of motor sizing on propeller specification and ESC and battery sizing on motor specification. The light cyan blocks correspond to the methodology stages, the dark blue blocks show requirements and constraints and the orange ellipses signify points of database access. The output data in green ellipses include specification parameters for sizing all of the major components of the propulsion system (namely propeller, motor, ESC, and battery) and the calculated propeller and motor operating points that can be used for calculating additional data, such as estimated flight time. The data corresponding to each of the outputs can be found in Table 2.

In Figure 6, a substantial impact of estimated total drone weight can be also seen—it is used to calculate required thrust T_r that plays a key role in selecting the propeller, and consequently the motor. Due to the discrete nature of propeller and motor parameters, the relationship is highly nonlinear, so it needs to be analysed numerically. However, it is easy to implement the methodology in a loop to plot the characteristics of flight time versus weight, which may be used in a payload sizing application.

3.2. Power System. The power system section of the methodology focuses on flight time estimation by modelling the battery. The model is based on the iterative approach presented

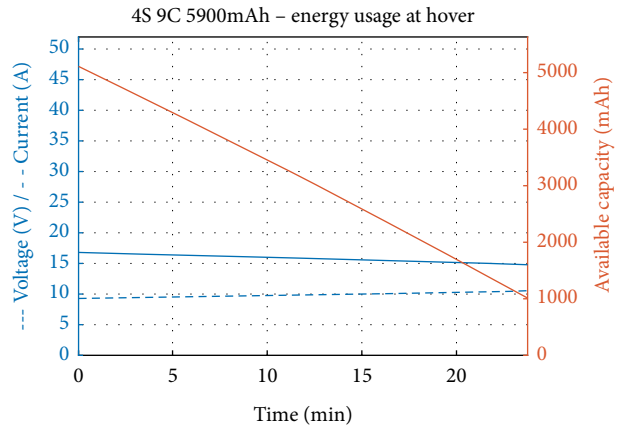

Figure 8: Example battery behaviour during hover.

by Traub [15]. It features two important phenomena—decrease of capacity with the increase of current and drop in voltage due to discharge. Additionally, the power demand can be varied throughout the simulation; however, in the base version of the methodology this is not used, as the operating points are constant. A block diagram of the calculations for one operating point can be seen in Figure 7.

Modelling of the battery capacity varying with drawn current is done through modified Peukert's equation in the form of:

$$t = \frac{Rt}{i^n}\left(\frac{C}{Rt}\right)^n, \tag{32}$$

where Rt is battery hour rating (1 hour in case of small packs) and n is Peukert's constant (1.3 for LiPo) dependent on battery type and temperature.

Measuring battery voltage is one of the main ways of measuring remaining charge in-flight. Typically, Lithium Polymer (LiPo) cells used in drones have 4.2 V when at full charge and drop to 3.7 V when at 20% charge. The voltage drop curve is nonlinear, but for the model it has been linearized and is expressed through

$$V(t) = V_0 - k_1[C_0 - C(t)], \tag{33}$$

Table 3: Errors between measured and simulated propeller characteristics—thrust coefficient (C_T) and power coefficient (C_P).

Mean C_T error	−0.0121
Mean relative C_T error	−12.6%
Mean std. deviation of C_T	0.0051
Mean C_P error	0.0059
Mean relative C_P error	2.48%
Mean std. deviation of C_P	0.0022

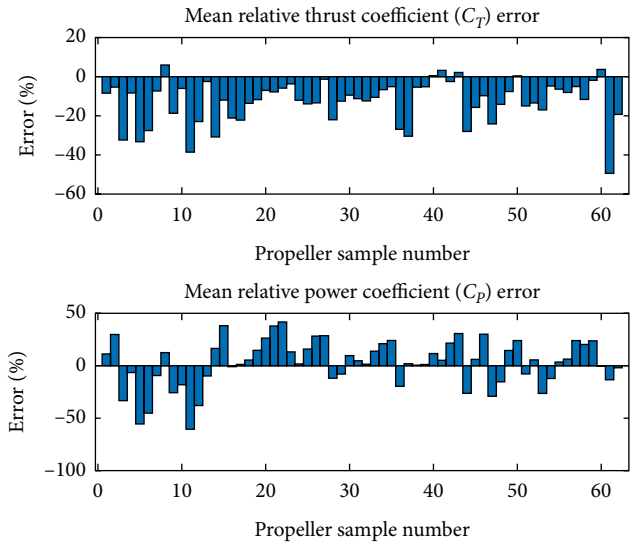

Figure 9: Relative errors between measured and simulated propeller coefficients.

$$k_1 = \frac{4.2\,\text{V} - 3.7\,\text{V}}{DoD \times C_0 \times n_C}, \tag{34}$$

where V_0 is the initial voltage, k_1 is the voltage drop coefficient, C_0 is the initial battery capacity, DoD is the maximal Depth of Discharge, and n_C is the number of battery cells. Based on Traub [15] the battery model can be defined with a set of iterative equations

$$V_{l+1} = V_0 - k_1[C_0 - C_l], \tag{35}$$

$$i_{l+1} = \frac{P_e}{V_{l+1}}, \tag{36}$$

$$C_{l+1} = i_{l+1}^{1-n} R t^{1-n} C^n - \sum_{m=1}^{l+1} i_m \Delta t \tag{37}$$

with the initial state defined as

$$V_0 = 4.2\,\text{V} \times n_C, \tag{38}$$

$$i_0 = \frac{P_e}{V_0}, \tag{39}$$

$$C_0 = i_0^{1-n} R t^{1-n} C^n. \tag{40}$$

The information flow in the model is visualized in Figure 7.

As time passes, the voltage decreases, therefore increasing current draw to achieve the same power, and consecutively decreasing available battery capacity due to Peukert's effect, as can be seen in Figure 8. The simulation is stopped when voltage reaches

$$V_e = 3.7\,\text{V} \times n_C \tag{41}$$

or when capacity reaches 20% of initial capacity (only works when power drawn is constant). The output is simply the simulation time, calculated as the product of the time step value and the number of iterations.

4. Example Results

The methodology presented has been implemented as a MATLAB script. This allows to easily process large quantities of data from propeller and motor databases and to plot component characteristics on every stage of the selection process.

In this example, performance data published by APC Propellers [16] will be used for the propeller database. It contains static and dynamic performance obtained through analytical methods of all products currently manufactured by the company. Due to the reliance on external computer software, airfoil drag (and consequently, torque) may be under-predicted at low speeds. Additionally, wind tunnel measurements of selected propellers [17] show overprediction of thrust coefficient (and consequently, thrust) of around 12% on average across all tested propellers. Detailed results are shown in Table 3 and in Figure 9. Therefore, an easily adjustable parameter called *Safety Factor* (*SF*) was introduced that increases required power at the WOT operating point to reduce the impact of mentioned inaccuracies and guarantee that the chosen motor will be able to reach the expected speed

$$I_j^{(2)} = P_m^{-1}(P_r \times SF), \tag{42}$$

$$\eta_j^{(2)} = \eta\left(P_r \times SF, P_{ej}\right). \tag{43}$$

There is no need to include *Safety Factor* in the ESC sizing, as the WOT operating point at which it is sized, in typical operating conditions, is achieved only for a few seconds at a time, not enough to damage the unit. The inclusion of the *Safety Factor* parameter in the battery sizing is recommended, as LiPo batteries are prone to ageing, which increases their internal resistance. Hence, with time at high currents more and more heat is generated, eventually leading to battery damage. What is more, cheap batteries are known for parameters varying between each unit, further justifying the need for an additional safety measure. Therefore, Equation (31) becomes

$$r_C = \frac{I_{\text{ESC}} \times n_{\text{rot}} \times SF}{C}. \tag{44}$$

For the motor database, a database bundled with Drive Calculator [2] software was used. It is based on measurements done and uploaded by its users, so it is impossible to accurately measure the discrepancies with real products, but they are estimated to be around 5–10% overall. However, a significant inaccuracy is introduced with the simplified motor model used

Table 4: Basic DJI Phantom 4 V2.0 parameters.

Number of rotors	4
Diagonal size	350 mm
Total weight	1375 g
Battery weight	468 g
Battery capacity	5870 mAh
Battery nominal voltage	15.2 V
Battery type	LiHV 4S
Propeller diameter	9 inch
Propeller pitch	5.5 inch

to calculate characteristics based on scarce data. The model, applicable both to BLDC and DC motors, considers only two sources of losses: copper losses, calculated using winding resistance

$$P_{\text{Cu}} = R_m I_{\text{motor}}^2 \tag{45}$$

and iron losses, calculated using no-load current

$$P_{\text{iron}} = V \times I_0, \tag{46}$$

where P_{Cu} are copper losses, R_m is the windings resistance (of all simultaneously working phases), I_{motor} is the current delivered to motor windings, P_{iron} are iron losses, V is the nominal voltage and I_0 is the no-load current. As the no-load measurement is usually done through an ESC, the iron losses also incorporate losses from the controller. The model, based on [18], is calculated as follows:

$$P_{\text{prop}} = \tau_{\text{prop}} \times \omega_{\text{prop}} \times SF, \tag{47}$$

$$I_{\text{motor}} = \frac{V - \sqrt{V^2 - 4R_m\left(P_{\text{iron}} + P_{\text{prop}}\right)}}{2R_m}, \tag{48}$$

$$P_{\text{motor}} = V \times I_{\text{motor}}, \tag{49}$$

$$\eta_{\text{motor}} = \frac{P_{\text{prop}}}{P_{\text{motor}}} \times 100\%, \tag{50}$$

where P_{prop}—is the power delivered to the propeller, τ_{prop} is the propeller torque, ω_{prop} is the propeller speed, P_{motor} is the motor electrical power, and η_{motor} is the motor efficiency.

To demonstrate the capabilities of the methodology a set of example results is presented for a low-weight drone. The results are validated against a similar commercial product. Based on the findings, a hypothetical usage of the methodology for sizing of Personal Air Vehicles is demonstrated.

4.1. Small Drone. For the ease of validation, the input parameters of the methodology were set to match those of the DJI Phantom 4 Pro V2.0, as indicated in Table 4. This enables easy comparison of the vehicle's published specification [19] with the sizing method's results in terms of flight time and propeller dimensions, as the manufacturer does not provide motor data. It should be noted here that the Phantom 4 uses LiHV (High Voltage LiPo) batteries rated at 3.8 V per cell, however in the calculations the more popular LiPo batteries, rated at 3.7 V per cell, are used. Additionally, V2.0 uses FOC-enabled drivers, which generate sinusoidal signals instead of the usual trapezoidal. However, the manufacturer advertises it as a means to reduce noise instead of improving performance, so it can be assumed that in this case the difference can be neglected.

Table 5: Additional methodology parameters used in small drone sizing.

Thrust-to-weight ratio r_T	3
Min. propeller diameter d_{min}	8 inch
Max. propeller diameter d_{max}	9 inch
Safety Factor SF	1.05
Preferred propeller series $\mathscr{S}_{n_r}$	MR, E, E-3, E-4
Max. propeller mass m_{p_r}	24 g
Max. motor mass m_{m_r}	100 g

The MATLAB script has been run considering two operating points: hover and WOT. The goal was to reduce energy usage at hover, as the platform's main purpose is photography. For the thrust the unit of gram-force (gf), which corresponds to the force acting on 1 gram of mass in a standard gravitational field, is used due to intuitiveness in this application. Additional sizing parameters are listed in Table 5. The results are below:

Results. For a 4-rotor drone with estimated AUM of 1375 g:

(i) APC 9×4.5E propeller should be chosen for the highest specific thrust of 9.69 gf/W per motor at hover.

(ii) Hacker B20 26L (2080 KV) motor should be selected with 0.15 Nm torque at maximum speed of 9600 RPM.

(iii) One motor uses 35 W of electrical power at hover and 237 W of electrical power at WOT.

(iv) The drive should be controlled by a 16 A ESC per motor.

(v) The whole system should be powered by a 4S 12C LiPo battery of 5870 mAh.

(vi) Hovering flight requires 124 W of mechanical power (0.05 Nm at 5600 RPM) to achieve 1375 gf of total thrust.

(vii) WOT flight requires 590 W of mechanical power (0.14 Nm at 9600 RPM) to achieve 4125 gf of total thrust.

(viii) This configuration should achieve around 26.9 min of hover and around 2.3 min of flight at WOT.

As can be seen, both the propeller and the motor were successfully selected and the estimated flight time has been calculated. The propeller is of lower pitch than in the reference drone, which might be explained by the unavailability of 9×5.5 propellers in APC's range, and 9×6 being too power-consuming. Especially interesting is the choice of E-series (electric airplanes) propeller over MR-series (multirotors),

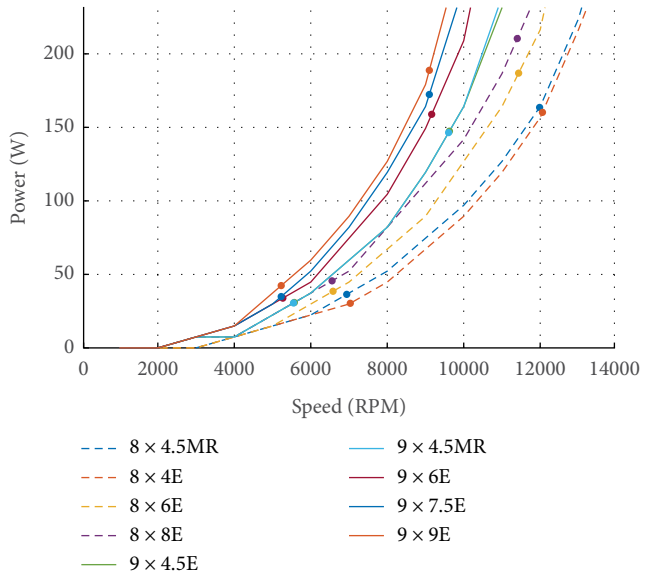

Figure 10: Comparison of power–speed characteristics of 8 and 9 inch propellers.

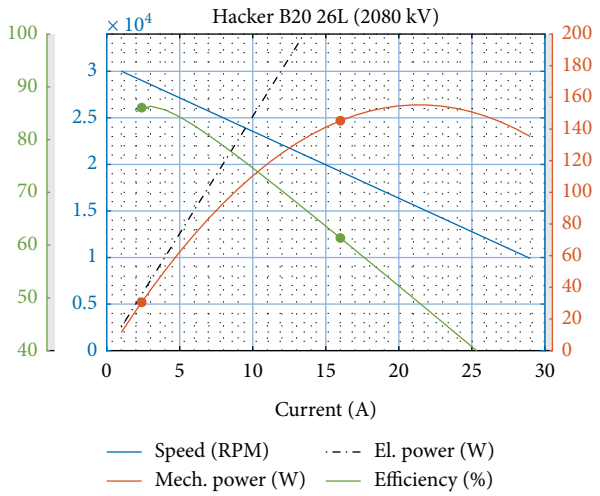

Figure 11: Simulated operating characteristics of Hacker B20 26L brushless motor.

which can be influenced by numerical errors due to interpolation, specifically at low speeds required for hovering. Comparison of power characteristics of propellers considered in this example can be seen in Figure 10.

Hacker B20 26L is a surprising choice for the application, as it is an inrunner motor that usually comes with gearing to increase its torque for traction applications. However, in this case it is used in direct drive configuration, which is possible due to the low speed of a large propeller. Its measured KV is 2080 (as opposed to 2020 stated by the manufacturer [20]), which puts the hover operating point almost at the maximum of the efficiency curve, therefore increasing the flight time, as can be seen in Figure 11.

The calculated flight time seems to be in line with the achievements of the reference drone. Maximum flight time

Table 6: Drone parameters used in further testing.

Name	GTQ Mini [8]	IRIS+ [21, 24]	PD6-AW2 BASIC [25]	Fox 4 [26]
Take-off mass [kg]	0.5	1.3	10	4
Thrust-to-weight ratio	2	2.6	3.5	2.5
Rotor count	4	4	6	4
Min. propeller diameter [inch]	3	8	18	10
Max. propeller diameter [inch]	5	10	21	15
Battery cell count	4	3	6	6
Battery capacity [mAh]	850	5100	2×16000	2×5000

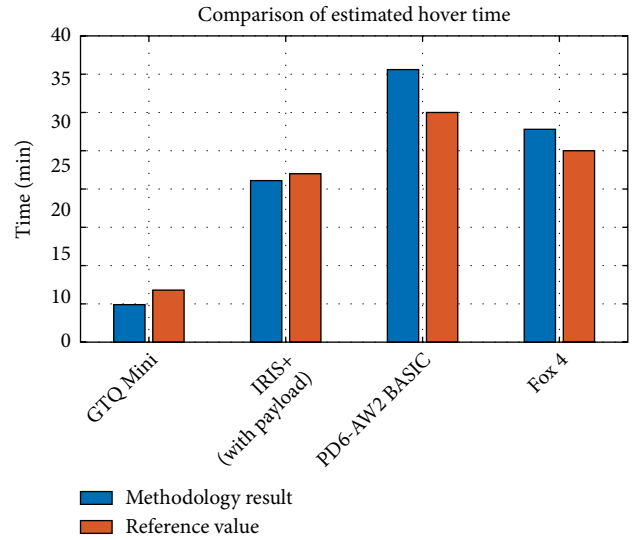

Figure 12: Comparison of calculated hovering time with longest expected time.

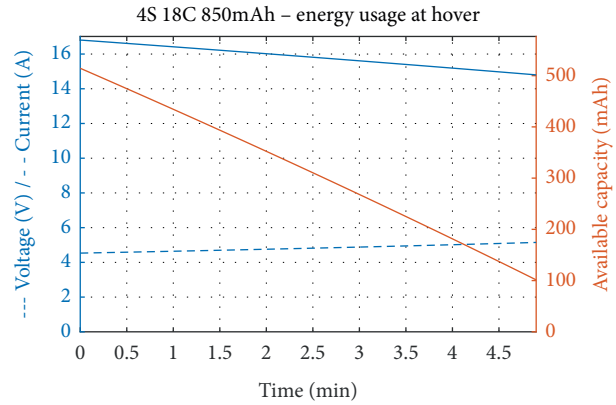

Figure 13: Battery behaviour of GTQ Mini during hover.

stated by the manufacturer is 30 min [19], but it was probably measured in flight at best endurance speed, which uses slightly less power than in hover ([21]) due to the reduction of the

Table 7: Uses of sizing methodology based on data available.

Propeller data	Motor data	Example uses
Available	Available	Complete sizing of multirotor propulsion system; flight time estimation; optimisation of flight time
Available	Not available	Propeller sizing; preliminary motor design
Not available	Available	Battery and ESC sizing; flight time estimation
Not available	Not available	—

induced drag. Therefore, it can be assumed that the maximum hover time will be close to the 27 min calculated, which seems to be confirmed by independent tests achieving 23–26 min of hover [22, 23]. However, as the calculations do not include dynamic effects of flight, the prediction accuracy for the WOT operating point is considerably lower. Furthermore, that point is set arbitrarily based on thrust-to-weight ratio, and is rarely measured in real operation, so no validation could be performed.

The reference drone is a commercially popular product, therefore it can be assumed that its performance is close to optimal for its given weight and application (aerial photography). Therefore, achieving results of similar value to the reference may indicate that the chosen configuration has performance close to optimal. Considering the accuracy of results, the assumptions and estimations used and the low computational cost, methodology performance can be considered satisfactory for applications in other research projects and on its own.

4.2. Further Validation. In similar manner to validation through comparison with DJI Phantom 4 v2.0, more tests of different configurations were conducted. The input parameters are summarised in Table 6. 6S batteries were assumed for Fox 4 and PD6-AW2 BASIC platforms, as those are more suited for the heavy lifting application. The weight of IRIS+ is taken with a sample payload. Thrust-to-weight ratio was adjusted so if more payload was added up to maximum allowable mass, the drone would still maintain controllability with thrust-to-weight ratio of 2. In 3 of the test cases, results shown in Figure 12 seem to be in satisfactory agreement with the manufacturer's specification considering that the methodology does not include the power usage by the flight controller, sensors, RC communication or payload.

The significant difference in the case of GTQ Mini needs to be addressed separately. The methodology has returned similar results to those of the methodology presented by Bershadsky et al. [8]. Our methodology has chosen 5×4.3 propellers as compared to 5×3, 1378 KV motor as compared to 1383 KV and uses 4.54 A in hover (at full battery) as compared to 4.49 A. However, there is a 1.9 min difference in calculated hover times. With the same battery capacity and similar current drawn, the discrepancy might be that in [8] the simulation is stopped when battery reaches 3.6 V, while our implementation is set up to stop earlier at 3.7 V. Another difference is probably in the battery model used, as our methodology simulates the decrease of voltage with discharge, leading to the increase in current drawn from 4.54 A to 5.15 A throughout battery operation, as can be seen in Figure 13.

4.3. Personal Air Vehicle. The current implementation of the methodology as a MATLAB script does not allow the sizing of heavy platforms, such as PAV, due to the lack of a sufficiently large propeller in database. However, the methodology can be implemented with different databases and even modified to help with the design of components: propeller specification provides enough data for presizing of an electric motor, and thrust requirements along with size and weight constraints can be used as input in propeller design. Additionally, using only scarce data, a flight time estimation can be performed to validate the design of components. This is an especially important feature, as the methodology has been designed with the ability to be used inside another algorithm to further enhance the optimisation process. That way questions, such as rotor number, propeller, size or maximum payload, can be answered. This is especially important for PAV, where the mass constraint is very tight because of the payload in the form of a passenger. Table 7 outlines example uses of the methodology in scenarios with different data available.

Some of the problems of Personal Air Vehicles, such as high weight of the platform, can be addressed by alternative multirotor designs. Papa [27] discusses a multirotor in which a part of the lifting is done by a balloon. Our methodology is simple and flexible enough to complement the approach in [27]. Papa's method can be used for sizing the balloon while our methodology sizes the multirotor part by subtracting the calculated balloon's lift from the estimated platform's weight and using it as an input. Validation of this approach, however, needs to be performed.

5. Conclusion

The methodology presented in this paper answers the need to have an automated process of selecting multirotor components using a simple input of estimated drone weight. Validation was performed using data from four commercially available multirotors (including DJI Phantom 4 V2.0) and one specialised platform, which shows that the obtained results are in accordance with manufacturer data and independent tests.

The simplicity and open-loop approach are also the limitations of this methodology. The use of static model does not provide enough information to estimate the acceleration, turn speed or performance in wind conditions. However, the inclusion of a dynamic model would require the bandwidth limitations of the actuators to be considered. This would overly increase the complexity of the methodology and would demand much more input data, thus limiting the usability.

Although there are no conceptual constraints preventing the use of the methodology for sizing large passenger multirotors, considerable limitations are introduced by the

databases used, which rarely provide data on large propellers in the 50–60 inch range and motors able to support them. However, it is assumed, that certain elements of the methodology, such as flight time estimation based on limited data, can be useful in the process of PAV design. Finally, the proposed methodology is also flexible enough to accept data of custom designed components or to be used for sizing of certain alternative multirotor topologies.

Unfortunately, one of the most important disadvantages of this methodology is its low, hard to estimate, accuracy. Great care was taken to make the results as close to reality as possible, but due to assumptions made for the sake of simplicity and speed, such as the use of thrust-to-weight ratio instead of calculation of maximum required thrust, the accuracy of calculations is impossible to measure. If needed, it can be enhanced, for example by improving motor model or using databases with only measured data, but it is advised against relying on the results in safety-critical applications.

Data Availability

The MATLAB code used to support the findings of this study have been deposited in the GitHub repository (https://github.com/mbiczyski/Multirotor-Sizing-Methodology). APC propeller performance data used to support this study is available at https://www.apcprop.com/technical-information/performance-data/. These datasets are cited at relevant places within the text as reference [12]. Previously reported propeller experimental performance data were used to support this study and are available at http://m-selig.ae.illinois.edu/props/propDB.html. These prior studies (and datasets) are cited at relevant places within the text as reference [14]. Motor performance data used to support this study is available at http://www.drivecalc.de/. These datasets are cited at relevant places within the text as reference [3].

Conflicts of Interest

The authors declare that there have no conflicts of interest.

Funding

Research and publication of the article was funded by ESTACA, France, and Cranfield University, UK.

References

[1] G. Szafranski, R. Czyba, and M. Blachuta, "Modeling and identification of electric propulsion system for multirotor unmanned aerial vehicle design," in *2014 International Conference on Unmanned Aircraft Systems*, pp. 470–476, IEEE, Orlando, FL, USA, 2014, ICUAS 2014 - Conference Proceedings.

[2] C. Persson, "Drive calculator," 2019, http://www.drivecalc.de/.

[3] Solution for All Markus Müller, "eCalc - the most reliable electric motor calculator on the web for RC pilots," 2019, https://www.ecalc.ch/

[4] M. Gatti and F. Giulietti, "Preliminary design analysis methodology for electric multirotor," *International Federation of Automatic Control Proceedings Volumes*, vol. 46, no. 30, pp. 58–63, 2013.

[5] M. Gatti, "Complete preliminary design methodology for electric multirotor," *Journal of Aerospace Engineering*, vol. 30, no. 5, p. 9, 2017.

[6] M. Kim, H. Joo, and B. Jang, "Conceptual multicopter sizing and performance analysis via component database," in *2017 Ninth International Conference on Ubiquitous and Future Networks (ICUFN)*, vol. 7, pp. 105–109, IEEE, Milan, Italy, 2017.

[7] P. M. Basset, A. Tremolet, and T. Lefebvre, "Rotary wing UAV pre-sizing : past and present methodological approaches at Onera," *Aerospace Lab*, vol. 8, pp. 1–12, 2014.

[8] D. Bershadsky, S. Haviland, and E. N. Johnson, "Electric multirotor UAV propulsion system sizing for performance prediction and design optimization," in *57th AIAA/ASCE/AHS/ASC Structures, Structural Dynamics, and Materials Conference*, vol. 1, pp. 1–22, American Institute of Aeronautics and Astronautics, Reston, Virginia, 2016.

[9] X. Dai, Q. Quan, J. Ren, and K.-Y. Cai, "An analytical design-optimization method for electric propulsion systems of multicopter UAVs with desired hovering endurance," *IEEE/ASME Transactions on Mechatronics*, vol. 24, no. 1, pp. 228–239, 2019.

[10] X. Dai, Q. Quan, J. Ren, and K.-Y. Cai, "Efficiency optimization and component selection for propulsion systems of electric multicopters," *IEEE Transactions on Industrial Electronics*, vol. 66, no. 10, pp. 7800–7809, 2019.

[11] O. Magnussen, M. Ottestad, and G. Hovland, "Multicopter design optimization and validation," *Modeling, Identification and Control*, vol. 36, no. 2, pp. 67–79, 2015.

[12] J. M. Miller, "Energy storage technologies," *Propulsion Systems for Hybrid Vehicles*, pp. 439–522, Institution of Engineering and Technology, 2010, chapter 10.

[13] Half Chrome Drones, "Drone thrust testing," 2019, https://www.halfchrome.com/drone-thrust-testing/.

[14] O. Liang, "How to choose motor for racing drone & quadcopter," 2019, https://oscarliang.com/quadcopter-motor-propeller/.

[15] L. W. Traub, "Range and endurance estimates for battery-powered aircraft," *Journal of Aircraft*, vol. 48, no. 2, pp. 703–707, 2011.

[16] APC Propellers, "Performance data," 2019, https://www.apcprop.com/technical-information/performance-data/.

[17] J. B. Brandt, R. W. Deters, G. K. Ananda, and M. S. Selig, "UIUC propeller database," 2019, http://m-selig.ae.illinois.edu/props/propDB.html.

[18] Radio Control Info, "Brushless motor efficiency and constants," http://www.radiocontrolinfo.com/brushless-motor-efficiency/

[19] DJI, "DJI Phantom 4 Pro V2.0.," 2019, https://www.dji.com/phantom-4-pro-v2.

[20] Hacker, "B20 26 L kv2020 + 4:1," https://www.hacker-motor-shop.com/Brushless-Motors/Hacker-Inrunner/Hacker-B20/B20-L-with-Gears/B20-26-L-kv2020-4-1.htm?shop=hacker_e&SessionId=&a=article&ProdNr=10017700&p=2072&rdeocl=1&rdetpl=categorypage&rdebox=box4/.

[21] C. Di Franco and G. Buttazzo, "Energy-aware coverage path planning of UAVs," in *2015 IEEE International Conference on Autonomous Robot Systems and Competitions*, pp. 111–117, IEEE, Vila Real, Portugal, 2015.

[22] T. Luna, "DJI Mavic 2 Pro vs. Phantom 4 Pro v2.0!," 2018, May 2019, https://www.wetalkuav.com/dji-mavic-2-pro-vs-phantom-4-pro-v2-0/.

[23] K. Smith, "DJI Mavic Pro VS Phantom 4 Pro V2. 0: which drone is better?" 2018, May 2019, https://myfirstdrone.com/blog/dji-mavic-pro-vs-phantom-4-pro-drone-better/.

[24] Arducopter, "Iris RTF quadcopter UAV support - Arduino based Arducopter UAV, the open source multi-rotor," 2019, September 2019, http://www.arducopter.co.uk/support.html.

[25] Prodrone, "PD6-AW2 BASIC," September 2019, https://www.prodrone.com/products/pd6-aw2-basic/.

[26] Hélicéo, "Multirotor drone for professionals, surveyors & topographers Fox4," 2019.September 2019, http: //www.heliceo.com/en/produits-pour-geometres/fox4-multirotor-drone/.

[27] U. Papa, *Embedded Platforms for UAS Landing Path and Obstacle Detection*, vol. 136 of *Studies in Systems Decision and Control*, Springer International Publishing, 2018, cham.

Hindawi
Journal of Advanced Transportation
Volume 2020, Article ID 1456207, 10 pages
https://doi.org/10.1155/2020/1456207

WILEY | Hindawi

Research Article

Trajectory Planning Method for Mixed Vehicles Considering Traffic Stability and Fuel Consumption at the Signalized Intersection

Shan Fang, Lan Yang, Tianqi Wang, and Shoucai Jing

College of Information Engineering, Chang'an University, Xi'an, Shanxi 710064, China

Correspondence should be addressed to Lan Yang; lanyang@chd.edu.cn

Received 26 July 2019; Accepted 9 November 2019; Published 10 January 2020

Guest Editor: Xiaobo Qu

Traffic lights force vehicles to stop frequently at signalized intersections, which leads to excessive fuel consumption, higher emissions, and travel delays. To address these issues, this study develops a trajectory planning method for mixed vehicles at signalized intersections. First, we use the intelligent driver car-following model to analyze the string stability of traffic flow upstream of the intersection. Second, we propose a mixed-vehicle trajectory planning method based on a trigonometric model that considers prefixed traffic signals. The proposed method employs the proportional-integral-derivative (PID) model controller to simulate the trajectory when connected vehicles (equipped with internet access) follow the optimal advisory speed. Essentially, only connected vehicle trajectories need to be controlled because normal vehicles simply follow the connected vehicles according to the Intelligent Driver Model (IDM). The IDM model aims to minimize traffic oscillation and ensure that all vehicles pass the signalized intersection without stopping. The results of a MATLAB simulation indicate that the proposed method can reduce fuel consumption and NO_x, HC, CO_2, and CO concentrations by 17%, 22.8%, 17.8%, 17%, and 16.9% respectively when the connected vehicle market penetration is 50 percent.

1. Introduction

Urban traffic flow is frequently interrupted by sharp acceleration and deceleration of vehicles at signalized intersections. Such stop-and-go traffic caused by unsafe driving behaviours not only influences the stability of the traffic flow but also leads to high crash risks. Furthermore, vehicle fuel consumption and emissions are dramatically increased when vehicles slow down or idle, and excessive travel delays become more likely.

With increasing technological developments, a vast array of intelligent transportation methods has been proposed to solve this problem. For example, Rakha & Kamalanathsharma [1] used such methods to improve fuel consumption efficiency when vehicles approach a signalized intersection. Liu et al. [2] proposed a method enabling autonomous vehicles to pass through an intersection without idling; this method was implemented by establishing an intersection management system that assigns reasonable priorities for all present vehicles. Yang et al. [3] proposed an eco-driving algorithm that instructs a driver how to pass through an intersection smoothly without stop-and-go behavior. Yao et al. [4] designed a trajectory smoothing method based on individual variable speed limits with location optimization in coordination with prefixed signals. Qu et al. [5] proposed a new method based on the weighted least square that can describe the speed-density or flow-density relationship of the empirical data precisely. Furthermore, he applies a new calibration approach to produce the random traffic flow fundamental diagrams [6], the ensuing experiment indicated that the proposed approach could fit the real speed-density data and derive the speed distributions according to the different given densities. Zhou et al. [7] investigated the characteristic of the oscillation at the signalized intersection, proposed a data driven car following model; this model had a high accuracy under oscillation and could distinguish the attribution of the drivers. Ding et al. [8] designed a method to predict the potential for yellow-light or red-light-running and determine a balance between algorithm efficiency and computational time. Levin and Rey [9] developed a reservation-based intersection control protocol and improved its applicability to situations with a large number of vehicles. Li et al. [10] proposed

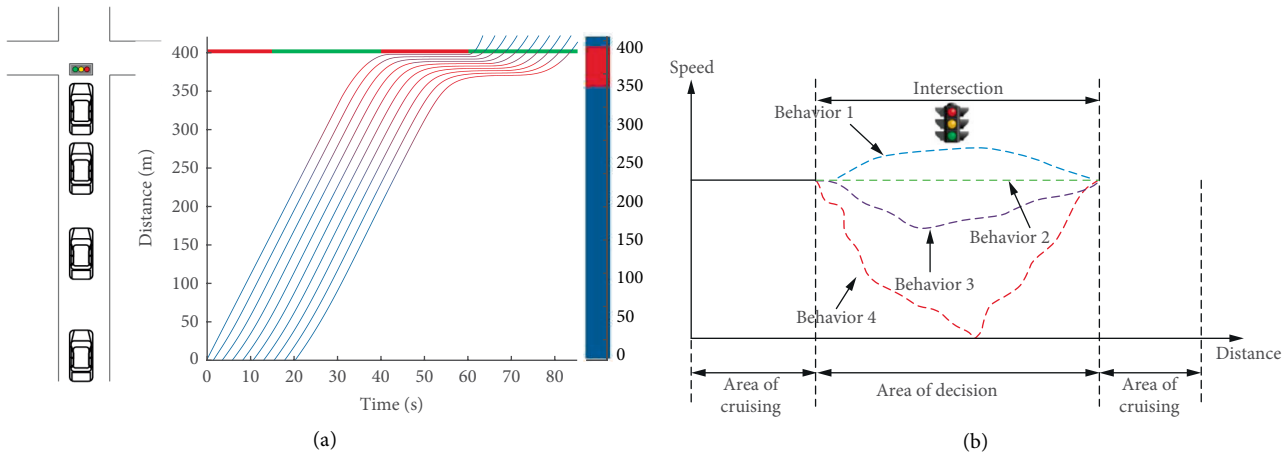

(a) (b)

FIGURE 1: Illustration of (a) a congested signalized intersection and (b) different unsafe driving behaviours.

a trajectory planning method based on shooting heuristic [11, 12] with a piecewise function; the simulation revealed that the model could decrease the stop-and-go movements. In order to solve the connected infrastructure design problem, 2 linear models were proposed by Li et al. [13]. The set of tests showed that the presented model had a better performance. Xu et al. [14] presented a new energy consumption index and generalized regression neural network respectively to describe the relationship between the truck fuel consumption and drivers' driving behavior. The experiment indicated that the two models could predict the fuel consumption accurately. Amir el al. [15] developed a mixed traffic speed harmonization model with connected autonomous vehicles and conducted sensitivity analysis and multi-lance scenario test. Bichiou and Rakha [16] transferred the best vehicle speed problem at an intersection into a constrained optimal problem. Lee and Park [17] proposed a connected-vehicle sensing algorithm for an intersection based on vehicle-to-infrastructure (V2I) technology. Jiang et al. [18] built an optimal control method for a signalized intersection, which obtains optimal speed through the minimum principle. Jing et al. [19] proposes a new approach to reduce oscillation and fuel consumption. Ma et al. [20] reviewed a number of speed harmonization methods and investigated performance of the methods in real traffic. Stacy el al. [21] proposed new method of the freeway speed harmonization experiment based on the Internet of Vehicle; the real experiment of the I-66 freeway indicated it can reduce the traffic oscillation. Guo et al. [22] proposed a joint optimization of vehicle trajectories and intersection controllers, two different strategies were investigated to control trajectory and control intersection, respectively. Hale et al. [23] compared different signal timing optimization methods and observed the best performance in the heuristic algorithm based on V2I technology. Zhao et al. [24] proposed a connected-vehicle control strategy for a signalized intersection that employs model prediction control to guide connected vehicles. Finally, Feng et al. [25] proposed a joint control method of vehicle trajectories and traffic signals for connected and automated vehicles at a signalized intersection.

However, none of these studies acknowledge the very likely scenario that a driver may not follow the recommended speed strategy because of a complex real-life environment. Therefore, this study attempts to solve previous problems related to trajectory planning at signalized intersections. First, we utilize the Intelligent Driver Model (IDM), a type of car-following model [26], to theoretically evaluate traffic oscillations at signalized intersections. Second, we propose a mixed-vehicle trajectory planning method (MVTPM). This method provides an optimal advisory speed strategy based on current vehicle status and signal phase and timing information (SPaT), then uses a proportional-integral-derivative (PID) controller to simulate trajectories when drivers follow the speed strategy. This study has the following four objectives: (1) to analyze traffic oscillation at signalized intersections; (2) to simplify the vehicle speed control strategy to only consider a few key variables; (3) to use the PID controller to simulate trajectories; and (4) to perform numerical experiments to verify the efficiency of the proposed MVTPM.

This study assumes that there is no delay in data transmission loss between communication in the control area, overtaking, and lane changing behavior is also not considered. Although these assumptions are too ideal to replicate transportation environments, the results from this ideal scenario can reveal potential connected and automated vehicle (CAV) technologies for improving existing problems in traffic systems.

This paper is organized as follows. Section 2 describes the key problems in the research field. Section 3 introduces the proposed mixed-vehicle trajectory planning method. Section 4 evaluates the passing efficiency and fuel consumption of the method using numerical experiments and Section 5 concludes this paper.

2. Problem Descriptions

2.1. Congested Signalized Intersection Problem. The traffic environment of a signalized intersection is very complex and characterized by vehicles idling while they wait to pass through the intersection, as shown in Figure 1(a). Many drivers do not know whether they can pass through the intersection before the traffic light turns red, so they perform unsafe driving behaviors, which leads to increased fuel consumption of

vehicles at the intersection. These unsafe driving behaviors can be divided into four types: "Acceleration," "Cruise," "Deceleration," and "Idle" (Figure 1(b)). In addition, when the vehicle is running in idle, the engine speed is very low, so the fuel cannot be fully burned, discharging a large amount of carbon dioxide (CO_2), hydrocarbons (HC), carbon monoxide (CO), nitrogen oxide (NO_x), and other harmful and toxic gases, which can seriously affect the ecological environment.

In this study, the VT-Micro [27] fuel consumption model is employed to calculate the indexes of vehicle fuel consumption and emissions, such NO_x, HC, CO_2, and CO. To the best of our knowledge, there are some fuel consumption models, they are VT-Micro, Motor Vehicle Emission Simulator (MOVES), vehicle specific power (VSP) respectively. The MOVES model utilizes the concept of the VSP distributions to calculate fuel consumption and pollution. However, if we use default VSP distributions of the MOVES, it may lead to many mistakes. Besides, we just care about the performance of the proposed system and do not consider other nonrelevant factors, such as weather-related, vehicle-related, road-related etc. The VT-Micro use the vehicle's instantaneous speed and acceleration levels to estimate vehicle emissions, and our system's target is trajectory planning of the connected vehicle based on the acceleration and velocity, so it fits our requirement of the fuel consumption model. VT-Micro is a polynomial regression model, which is a function of acceleration and speed, and expressed as follows:

$$\mathrm{MOE} = \exp\left(\sum_{i}^{3}\sum_{j}^{3} k_{i,j} \times v \times a\right), \tag{1}$$

where $k_{i,j}$ is the correlation coefficient, v is the velocity, and a is the acceleration. However, this fuel consumption model cannot calculate CO_2, which is a key emission. Nevertheless, fuel consumption and CO_2 emissions are related [28] by the following function:

$$\mathrm{CO}_2 = \alpha_1 v + \alpha_2 \mathrm{MOE}, \tag{2}$$

where α_1 and α_2 are coefficients and MOE is the fuel consumption.

The Xiaozhai intersection (Xi'an, China) is used as an example to illustrate the fuel consumption problem at a signalized intersection (Figure 2). The red-light time of the intersection is 100 s and the green-light time of the intersection is 40 s. First, we use a digital video camera on top of a bridge to count the number of idling cars (only considering straight-through vehicles) and calculate the fuel consumption. Second, we compare it with the fuel consumption of nonidling cars.

In the paper, we define the congested period is 08:00–09:00, one hour. During this time, the number of the passed vehicles is 1425. The traffic volume of the congested period is 1425/1 = 1425 pcu/h. We also define the uncongested period is 09:00–11:00, two hours. During this time, the number of the passed vehicles is 1478. The traffic volume of the uncongested is 1478/2 = 739 pcu/h. And we calculate the fuel consumption and pollution of the different period. According to Table 1, the fuel consumption and emissions were higher for the congested period, thus, this study aims to optimize vehicle speed and fuel consumption at a signalized intersection.

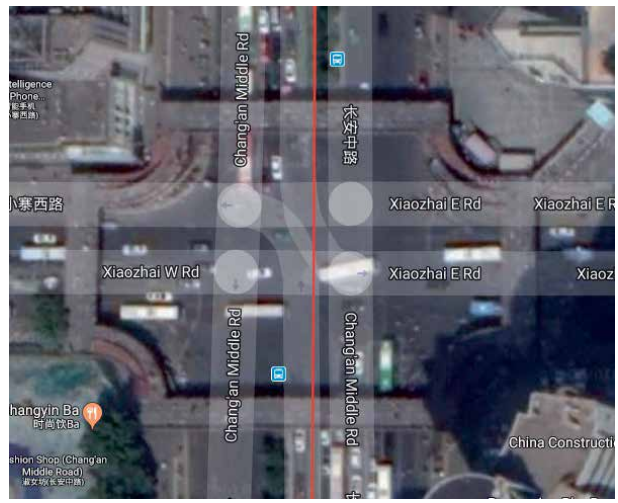

Figure 2: XiaoZhai Intersection in Xi'an, China.

2.2. The Stability Analysis Problem of the Car-Following Model. In general, the mathematical expression for the traditional car-following model is defined as

$$a_n = f(v_n, \Delta v_n, \Delta x_n), \tag{3}$$

where a_n, v_n, Δv_n, and Δx_n represent the nth vehicle's acceleration, speed, relative speed, and headway respectively. From Equation (3), we can first obtain the vehicle's acceleration then obtain the speed and distance using the integral to simulate the nth vehicle's trajectory.

There are two stability analyses in the car-following model: local stability and string stability. Local stability analysis mainly investigates the reaction of the vehicle to the fluctuation of the preceding vehicle's speed, focusing on local behaviour between the two vehicles. String stability analysis mainly investigates the influence of speed fluctuations of the head vehicle on the overall dynamic characteristics of the vehicle fleet. For example, the IDM car-following model is expressed as follows:

$$a_n = \alpha\left[1 - \left(\frac{v_n(t)}{v_0}\right)^4 - \left(\frac{s_n^*(t)}{s_n(t)}\right)^2\right], \tag{4}$$

where the nth vehicle's acceleration, max acceleration, instant speed at time t, desired speed, gap, and desired gap at time t is denoted as a_n, α ,$v_n(t)$, v_0, $s_n(t)$, and $s_n^*(t)$, respectively. The expression for the desired gap $s_n^*(t)$ is:

$$s_n^*(t) = s_0 + \max\left(0, Tv_n + \frac{v_n(t)\Delta v_n(t)}{2\sqrt{\alpha\beta}}\right), \tag{5}$$

where s_0, T, $\Delta v_n(t)$, and β are the safe gap, reaction time, relative speed at time t, and comfort deceleration, respectively.

The local stability of the IDM car-following model is eternally stable [29]; thus, only the string stability of the IDM car-following model needs to be analysed. To linearize the nonlinear system with small perturbations at equilibrium time point h, we use a multivariate function first order Taylor

Table 1: Fuel consumption and emissions at XiaoZhai Intersection.

Intersection	Fuel (L)	CO_2 (kg)	CO (kg)	NO (kg)	HC (kg)
Congested	85.567	204.5861	1.0780	0.1396	0.0768
Uncongested	58.485	139.8460	0.7395	0.0785	0.0518

expansion to expand the acceleration function around the equilibrium point, as follows:

$$a(s, v, \Delta v) = a(s_h, v_h, \Delta v_h) + v_h'(v - v_h) + s_h'(s - s_h) + \Delta v_h'(\Delta v - \Delta v_h), \tag{6}$$

where s_h,v_h, and Δv_h denote the gap, speed, and relative speed at equilibrium point h; i.e.:, $v_h' = (\partial a/\partial v)|_h$, $s_h' = (\partial a/\partial s)|_h$, $\Delta v_h' = (\partial a/\partial \Delta v)|_h$. Furthermore, v_h', s_h', $\Delta v_h'$ are defined as below:

$$v_h' = \left.\frac{\partial a}{\partial v}\right|_h = -\alpha\left[\frac{4v_h^3}{v_0^4} + \frac{2T(s_0 + Tv_h)}{s_h^2}\right], \tag{7}$$

$$s_h' = \left.\frac{\partial a}{\partial s}\right|_h = \frac{2\alpha(s_0 + Tv_h)^2}{s_h^3}, \tag{8}$$

$$\Delta v_h' = \left.\frac{\partial a}{\partial \Delta v}\right|_h = \sqrt{\frac{\alpha}{\beta}}\frac{(s_0 + Tv_h)v_h}{s_h^2}. \tag{9}$$

The gap variation and speed variation are denoted as:

$$x_n = s_n - s_h, \tag{10}$$

$$y_n = v_n - v_h. \tag{11}$$

Thus, Equation (6) can be transformed into:

$$a(s, v, \Delta v) = a(s_h, v_h, \Delta v_h) + v_h' y_n + s_h' x_n + \Delta v_h'(y_{n-1} - y_n). \tag{12}$$

Then, we take the derivative with respect to x_n and y_n:

$$\dot{x}_n = \dot{v}_{n-1} - \dot{v}_n = \dot{y}_{n-1} - \dot{y}_n, \tag{13}$$

$$\dot{y}_n = s_h' x_n + (v_h' - \Delta v_h')y_n + \Delta v_h' y_{n-1}. \tag{14}$$

We consider the area upstream of the intersection as a linear system, where the transfer function is $G(i\omega)$, the speed disturbance of the first vehicle is $y_0 = e^{i\omega t}$, and the speed disturbance of the nth vehicle is $y_n = G^n(i\omega)e^{i\omega t}$. These terms are substituted into Equations (13) and (14):

$$-\omega^2 G^n(i\omega)e^{i\omega t} = s_h'\left(G^{n-1}(i\omega)e^{i\omega t} - G^n(i\omega)e^{i\omega t}\right) + (v_h' - \Delta v_h')i\omega G^n(i\omega)e^{i\omega t} = + \Delta v_h' i\omega G^{n-1}(i\omega)e^{i\omega t}, \tag{15}$$

$$G(i\omega) = \frac{s_n' + \Delta v_h' i\omega}{-\omega^2 + s_n' - i\omega(v_h' - \Delta v_h')}. \tag{16}$$

If the perturbation in a vehicle platoon is reduced rather than amplified, we have:

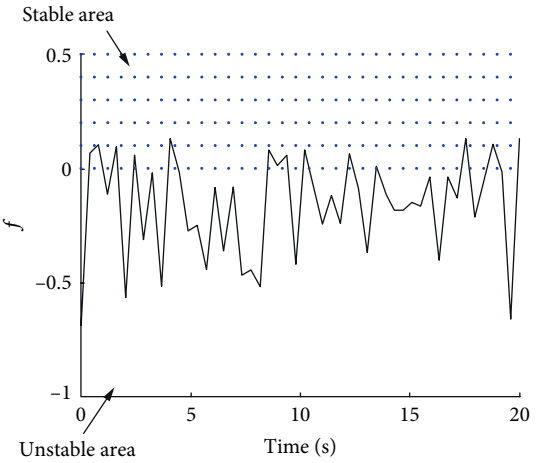

Figure 3: Traffic stability index for travel times of less than 20 s.

$$|G(i\omega)| = \frac{\sqrt{\omega^2(\Delta v_h')^2}}{\sqrt{(s_h' - \omega^2)^2 + \omega^2(v_h' - \Delta v_h')^2}} < 1. \tag{17}$$

Thus, the following inequation must be satisfied:

$$\omega^2(\Delta v_h')^2 + (s_h')^2 < (s_h' - \omega^2)^2 + \omega^2(v_h' - \Delta v_h')^2. \tag{18}$$

Because of the lower frequency, $\omega \to 0$, which is the stronger constraint on stability.

$$f = \frac{1}{2} - \frac{\Delta v_h'}{v_h'} - \frac{s_h'}{(v_h')^2} < 0. \tag{19}$$

Thus, the main reason for traffic flow instability is that the string stability is not satisfied. It is assumed that the vehicle speed fluctuates within a range of 8–12 m/s, and the gap fluctuates within a range of 20–30 m when the vehicle approaches the intersection. The instant velocity and gap of the vehicle are then substituted into Equation (19). The judgment expression is predominantly greater than zero, indicating that the traffic flow is in a stable state. However, as shown in Figure 3, the traffic flow is predominantly unstable for travel times of less than 20 s.

3. Mixed-Vehicle Trajectory Planning Method (MVTPM)

As shown in Figure 4, there are three units in the MVTPM: the input unit, control unit, and output unit. The input unit includes SPaT Information and vehicle status. SPaT information, obtained from DSRC Roadside, includes the signal phase and time. When a connected vehicle (i.e., a vehicle equipped with

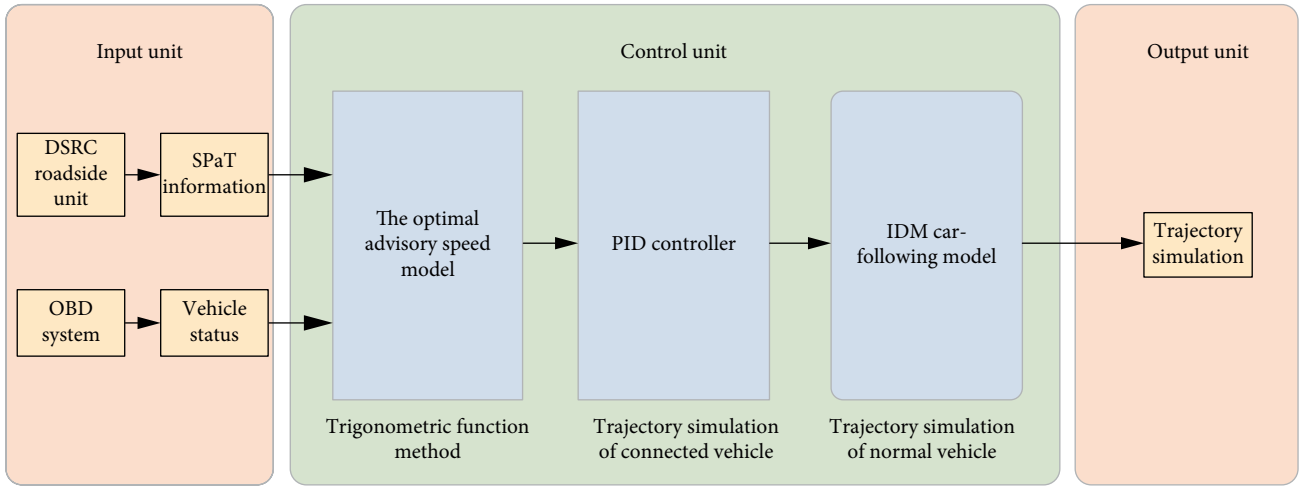

Figure 4: Mixed-vehicle trajectory planning method.

internet access) enters the control area upstream of the signalized intersection, the DSRC sends SPaT information to the connected vehicle. The vehicle status, which comes from OBD (on board diagnostics), includes vehicle current speed and acceleration and fuel consumption. The control unit includes three processes: the optimal advisory speed model is responsible for generating the optimal speed of connected vehicles based on the trigonometric function method; the PID controller simulates the trajectory when the driver follows the optimal speed advice; and the IDM car-following model simulates the trajectory followed by normal (nonconnected) vehicles. The output unit simulates the trajectory of mixed vehicles passing the signalized intersection from upstream to downstream.

3.1. Trigonometric Function Method. In this study, we employ the trigonometric function method to control the velocity of connected vehicles [30], which has many advantages such as smooth control and easy implementation. The trigonometric model is as follows:

$$v = \begin{cases} v1 = v_h - v_d \cos(st) & t = 0 \text{ to } \frac{\pi}{2s} \\ v2 = v_h - v_d \frac{s}{a} \cos\left(a\left(t - \frac{\pi}{2s} + \frac{\pi}{2a}\right)\right) & t = \frac{\pi}{2s} \text{ to } \left(\frac{\pi}{2a} + \frac{\pi}{2s}\right) \\ v3 = v_h + v_d \frac{s}{a} & t = \left(\frac{\pi}{2a} + \frac{\pi}{2s}\right) \text{ to } \frac{d}{v_a}, \end{cases} \tag{20}$$

where v_d denotes the speed difference, $v_d = |v_h - v_c|$, v_c represents the instantaneous speed of the connected vehicle entering the control area; v_h denotes the target maximum speed, the rate of change of acceleration in a different region is denoted as a, and s is the speed below the change in the deceleration rate of the target average speed.

The key to speed control is the velocity compensation mechanism, which states that the distance and time required for the connected vehicle to reach the intersection after entering the upstream control area is fixed. Thus, when the connected vehicle enters the control area slowly, the mechanism increases the distance by acceleration control. Similarly, when the connected vehicle enters the intersection rapidly, it decreases the distance by deceleration control. As shown in Figure 5, the enclosed area A should be equal to the sum of the enclosed area B1+B2.

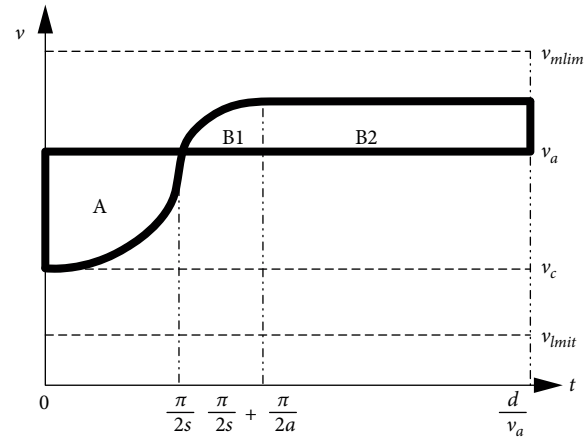

Figure 5: Schematic diagram of the distance compensation mechanism.

$$\begin{aligned} &\int_0^{\pi/2s} (v_h - v_d \cos(st))dt - \int_0^{\pi/2s} v_h dt \\ &= \int_{\pi/2s}^{\pi/2s+\pi/2a} \left(v_d \frac{s}{a} \cos\left(a\left(t - \frac{\pi}{2s} + \frac{pi}{2a}\right)\right) - v_a\right)dt \\ &\quad + \int_{\pi/2s+\pi/2a}^{d/v_a} \left(v_h + v_d \frac{s}{a}\right)dt - \int_{\pi/2s+\pi/2a}^{d/v_a} v_h dt. \end{aligned} \tag{21}$$

In Equation (21), a and s are the only unknown parameters so must be determined. The optimal solution of a and s is obtained by the following four limited conditions:

$$\begin{aligned} &\int_0^{\pi/2s} (v_h - v_d \cos(st))dt - \int_0^{\pi/2s} v_h dt \\ &= \int_{\pi/2s}^{\pi/2s+\pi/2a} \left(v_h - v_d \frac{s}{a} \cos\left(a\left(t - \frac{\pi}{2s} + \frac{pi}{2a}\right)\right)\right)dt \\ &+ \int_{\pi/2s+\pi/2a}^{d/v_a} \left(v_h + v_d \frac{s}{a}\right)dt - \int_{\pi/2s}^{d/v_a} v_h dt \\ &|v_h sa| \le 10 \\ &v_d s \le 2 \\ &s = \max\{s\} s = [0, 1]. \end{aligned} \tag{22}$$

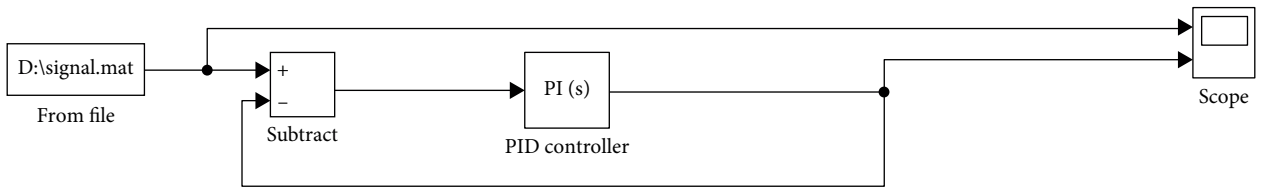

Figure 6: Diagram of the MATLAB Simulink program.

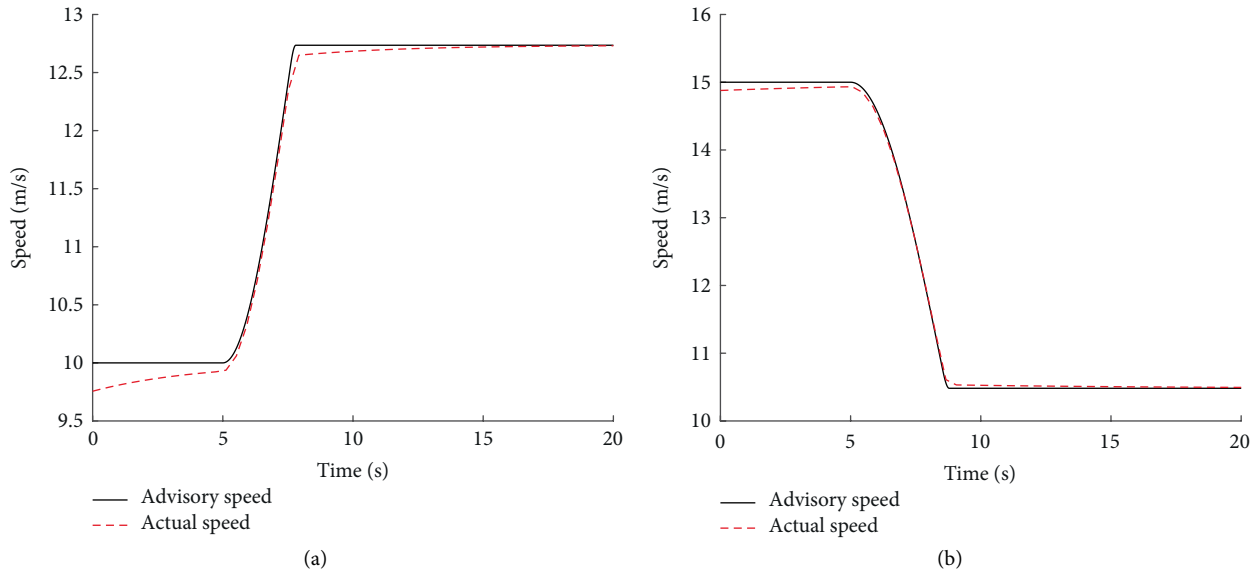

Figure 7: Driver response to optimal advisory speed: (a) acceleration and (b) deceleration.

The first condition is the distance compensation constraint mentioned above. The second and third conditions restrain the rate of change of acceleration and deceleration. According to economical connected-vehicle fuel consumption, in the fourth condition, fuel consumption is proportional to the speed control time; thus, the shorter the speed control time, the lower the fuel consumption. In trigonometric speed-guided expressions, variable s controls the speed-controlled completion; therefore, it must be qualified to the maximum value possible. In four constraints, there is only a and s unknown. To set s an initial value, use conditional one to obtain a, and then use the following three conditions to obtain the best solution.

3.2. Trajectory Planning of the Connected Vehicle. Many previous studies have focused on optimal speed control at a signalized intersection; however, few have considered the problem where a driver of a connected vehicle does not precisely follow the optimal advisory speed. The trajectory of a vehicle can vary enormously from the ideal trajectory because the speed control method is too complicated or impractical; therefore, it is necessary to determine the driver response to the optimal advisory speed. In this study, we use the PID model to simulate the driver's response when following the speed control method. The PID model is practical and simple, but its most important advantage is the clear physical meaning of the model parameters. That is, parameter P represents the time delay of the driver's behaviour, parameter I represents the accumulation of past errors, and parameter D represents the prediction of future errors. When the advisory speed is given, the driver pays more attention to the current difference; thus, we consider it a closed-loop model. Moreover, in order to simply the problem, we exclude the impact of the prediction of future errors and only consider the time delay and past errors. The diagram of the Simulink program in MATLAB is shown in Figure 6. Figure 7(a) shows the acceleration driver response, where the remaining green time is 20 s and the current velocity is 10 m/s. Figure 7(b) shows the deceleration driver response, where the remaining red light is 20 s and the current velocity is 15 m/s.

3.3. Trajectory Planning of the Normal Vehicle. The special conditions described by the co-existence of connected and normal vehicles in the traffic flow will continue for a long time in the foreseeable future. Therefore, it is necessary to improve the speed control algorithm to ensure that connected vehicles pass through the intersection without idling and normal vehicles follow connected vehicles through the intersection as much as possible. It is assumed here that the front vehicle of two vehicles in traffic flow is a connected vehicle and the rear vehicle is a normal vehicle. A mathematical model is established to describe their trajectory. Due to the trigonometric guidance method applied to the front vehicle, the driving trajectory model of the connected vehicle is obtained by the indefinite integral of the expression of the speed control function, as follows:

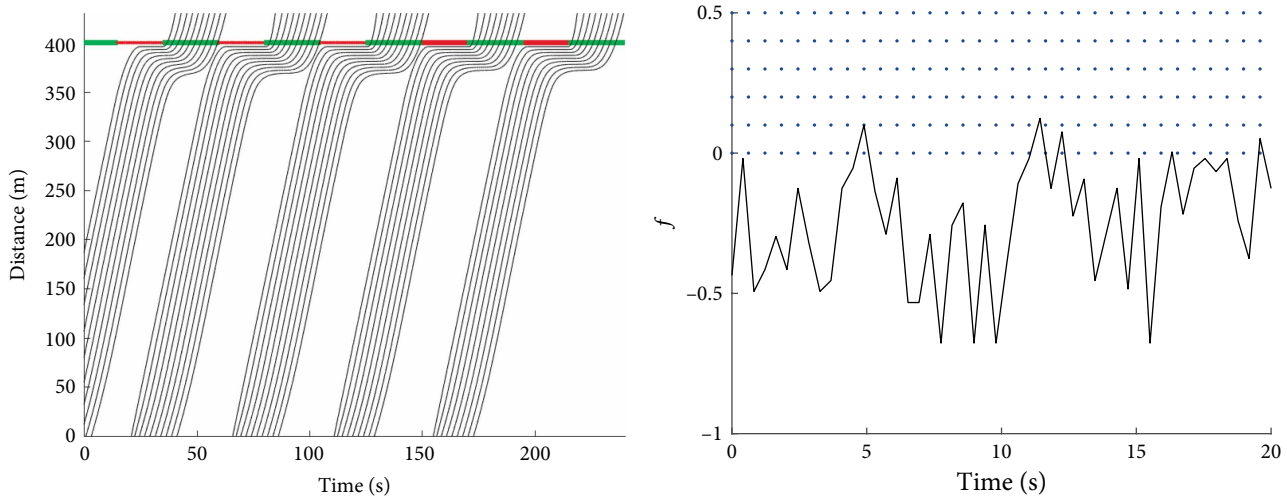

(a) (b)

Figure 8: Effect of a connected vehicle penetration rate of 0% on (a) the spatial-temporal trajectories for normal (black) and connected (red) vehicles and the stability index of the mixed-vehicle queue.

Table 2: Parameters used in simulation of the MVTPM.

Basic parameters	Value
Speed control area length	400 m
Maximum speed limit of the section	72 km/h
Minimum speed limit of the section	36 km/h
Vehicle initial speed	54.0–64.8 km/h
Green light time	35 s
Red light time	25 s
Connected vehicle market penetration rate	0–100%
Maximum acceleration of connected vehicle	2 m/s^2
Maximum deceleration of connected vehicle	−2 m/s^2
Maximum acceleration of normal vehicle	4 m/s^2
Maximum deceleration of normal vehicle	−4 m/s^2
Following car response time	2.5 s

$$d = \begin{cases} d_1 = v_h t - \frac{v_d}{s}\sin(st) & t = 0 \text{ to } \frac{\pi}{2s} \\ d_2 = v_h t - \frac{sv_d}{a^2}\sin a\left(t - \frac{\pi}{2s} + \frac{\pi}{2a}\right) & \\ +vd\left(\frac{s}{a^2} + \frac{1}{s}\right)t & t = \frac{\pi}{2s} \text{ to } \left(\frac{\pi}{2a} + \frac{\pi}{2s}\right) \\ d_3 = v_h t + v_d \frac{s}{a} t & \\ +v_d\left(\frac{s}{a^2} - \frac{1}{s} - \frac{\pi s}{2a^2} - \frac{\pi}{2a}\right) & t = \left(\frac{\pi}{2a} + \frac{\pi}{2s}\right) \text{ to } \frac{d}{v_a}. \end{cases} \quad (23)$$

When the normal vehicle enters the control area, the instantaneous speed of the normal vehicle is v, the distance is zero, and the entering time is t. At the same time, the instantaneous velocity of the connected vehicle is $v_h - v_d\cos(st)$ and the distance is $v_h t - (v_d/s)\sin(st)$. The following form is established in the IDM expression:

$$\mathrm{a} = a_{\max}\left[1 - \left(\frac{v_c}{v_{\max}}\right)^4 - \left(\frac{s_0 + \max v_c t + v_c\left(v_h - v_d\cos(st)\right)/2\sqrt{a_{\max} b_{dec}}}{v_h t - (v_d/s)\sin(st)}\right)^2\right]. \quad (24)$$

The velocity and position of the rear car is as follows [31]:

$$v_{n+1}(t + \Delta t) = v_n(t) + \frac{1}{2}\left(a_{n+1}(t) + a_{n+1}(t + \Delta t)\right)\Delta t, \quad (25)$$

$$d_{n+1}(t + \Delta t) = d_{n+1}(t) + v_{n+1}(t)\Delta t + \frac{a_{n+1}(t)(\Delta t)^2}{2}. \quad (26)$$

4. Simulation Evaluation

In this section, we conduct numerical experiments to illustrate the efficacy of the proposed MVTPM at a hypothetical intersection. The MVTPM was evaluated with a one factor sensitivity analysis using connected vehicle market penetration rates (MPRs). We assume that approximately 48 vehicles pass through the intersection and calculate the fuel consumption and emission of these vehicles using VT-Micro. The simulation parameters as shown in Table 2.

4.1. Trajectory Simulation. Figures 8–12 show the spatial-temporal trajectories for normal (black) and connected (red) vehicles with different connected vehicle market penetration rates and the stability index of the mixed-vehicle queue. Note that, at a lower penetration rate, many normal vehicles need to stop at the signalized intersection when the traffic light is red because there are not enough connected vehicles to guide them, leading to long waiting times and instability of the mixed-vehicle queue. However, with increasing market penetration of connected vehicles, the length of the queue is progressively shortened and the stability index increases to above zero.

4.2. Fuel Calculation. The proposed method is evaluated using the different MPRs, using the fuel consumption and concentrations of NO_x, HC, CO_2, and CO as measures of effectiveness. Table 3 confirms that the proposed MVTPM can optimize both objectives; i.e., reduce fuel consumption and vehicle emissions. Moreover, an increasing number of connected vehicles leads to further decreases in fuel consumption and emissions.

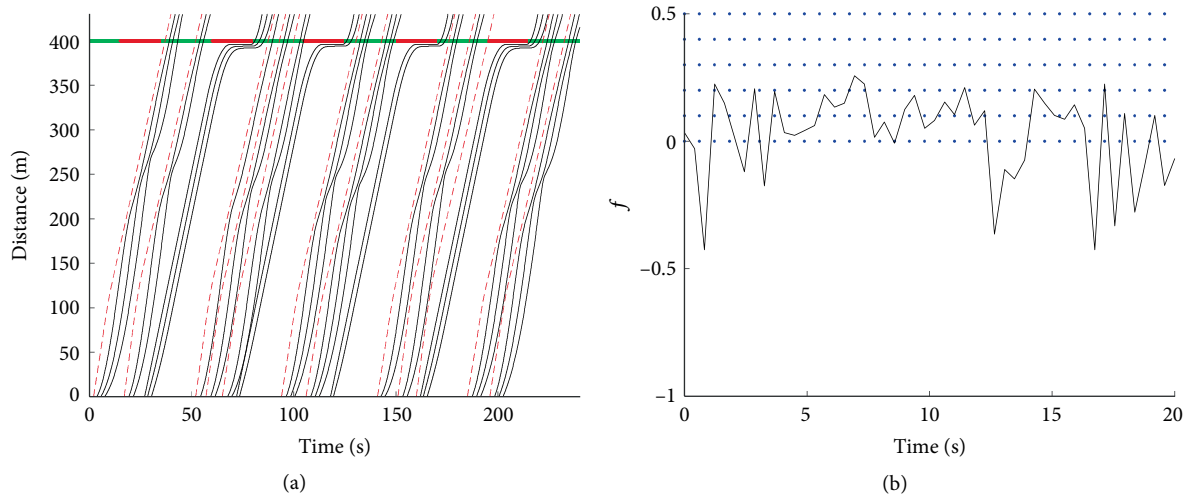

Figure 9: Effect of a connected vehicle penetration rate of 25% on (a) the spatial-temporal trajectories for normal (black) and connected (red) vehicles and the stability index of the mixed-vehicle queue.

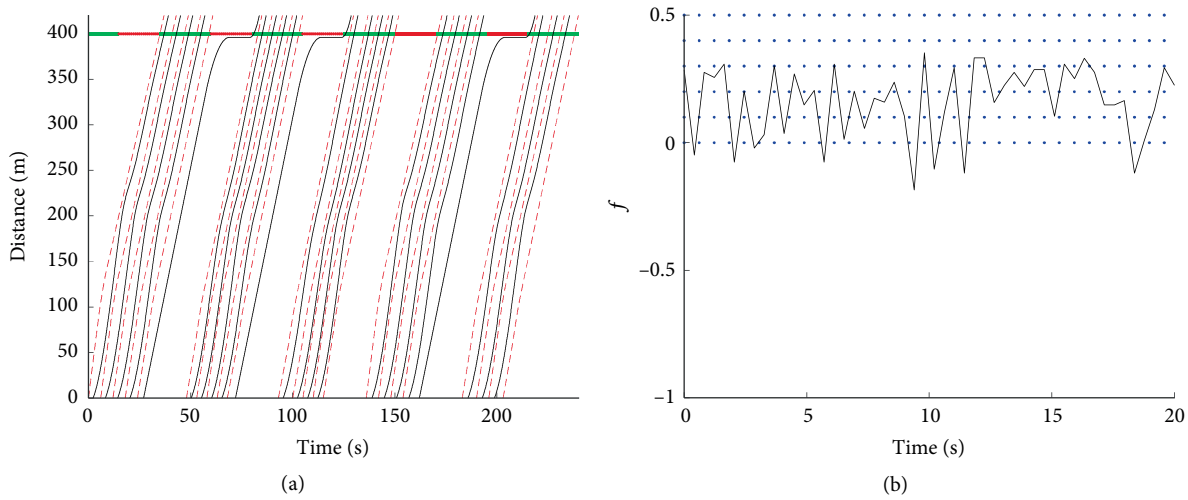

Figure 10: Effect of a connected vehicle penetration rate of 50% on (a) the spatial-temporal trajectories for normal (black) and connected (red) vehicles and the stability index of the mixed-vehicle queue.

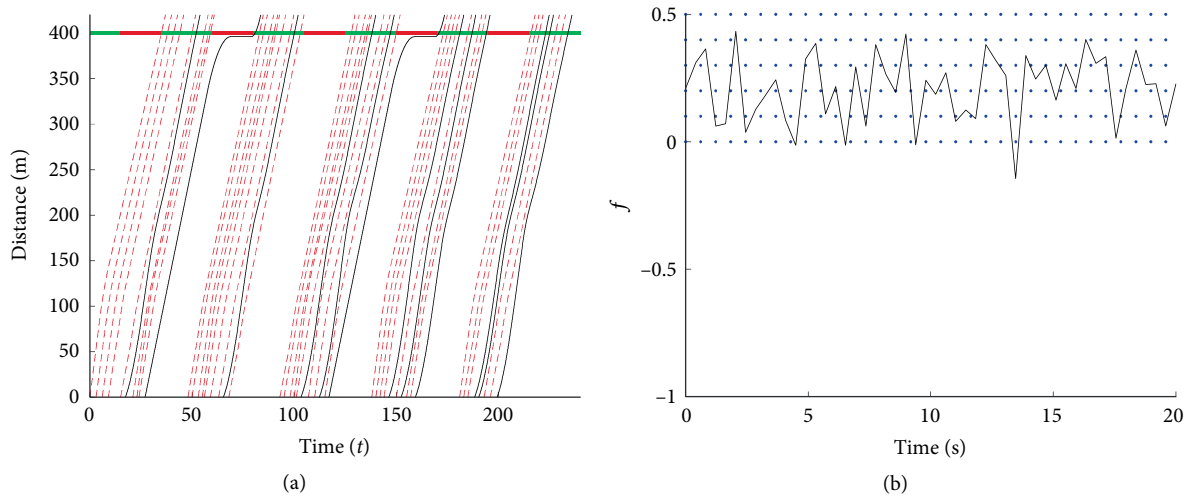

Figure 11: Effect of a connected vehicle penetration rate of 75% on (a) the spatial-temporal trajectories for normal (black) and connected (red) vehicles and the stability index of the mixed-vehicle queue.

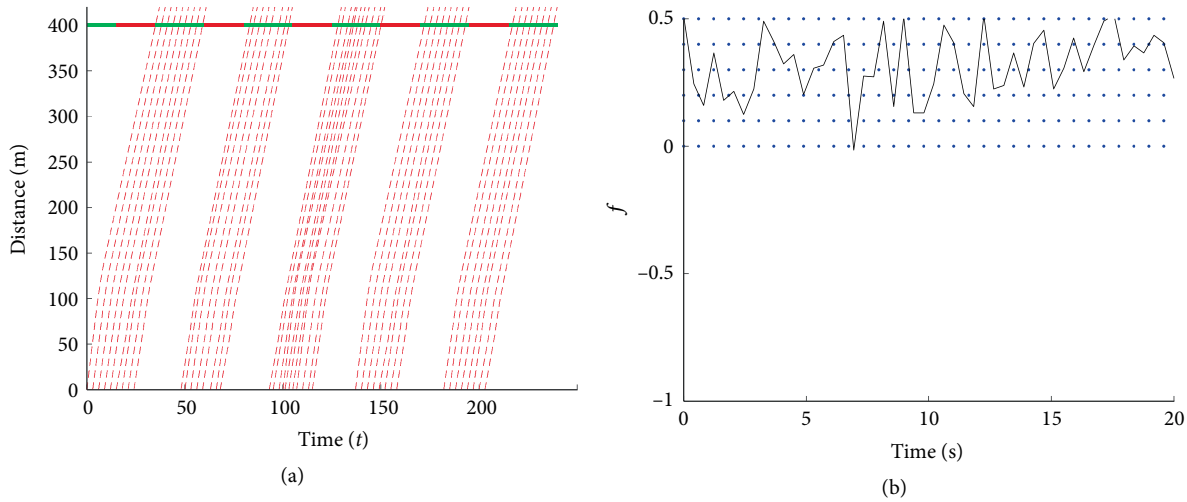

Figure 12: Effect of a connected vehicle penetration rate of 100% on (a) the spatial-temporal trajectories for normal (black) and connected (red) vehicles and the stability index of the mixed-vehicle queue.

Table 3: Fuel consumption and emissions of different MPRs.

Penetration rate	Fuel (L)	NO_x (mg)	HC (mg)	CO_2 (g)	CO (mg)
0%	2.88	4.70	2.59	6.89	36.31
25%	2.64	4.16	2.36	6.30	33.23
50%	2.39	3.63	2.13	5.72	30.16
75%	2.15	3.09	1.91	5.13	27.1
100%	1.9	2.55	1.68	4.54	24.02

5. Conclusion

This study analyzes the mechanism of traffic oscillations at signalized intersections from the perspective of string stability; then proposes a mixed-vehicle trajectory planning method using the triangular-function method to optimize the speed of connected vehicles in the mixed traffic flow. Moreover, the PID controller is used to simulate the trajectory of connected vehicles; and the IDM car-following model is used to optimize the speed of normal vehicles. MATLAB simulations reveal that the proposed trajectory planning method successfully reduces fuel consumption and emissions for the vehicles passing through a signalized intersection. When the market penetration rates of connected vehicles is 100%, the fuel consumption and NO_x, HC, CO_2, and CO concentrations decrease by 34%, 45.7%, 35.1%, 34.1%, and 33.9%, respectively. Future research should focus on improving fuel consumption, vehicle emissions, and vehicle passing efficiency at continuous signalized intersections in urban areas.

Data Availability

This research is all based on the simulation of the MATLAB, no data were used to support this study.

Conflicts of Interest

The authors declare that there is no conflicts of interest regarding the publication of this paper.

Authors' Contributions

The authors confirm contribution to the paper as follows: study conception and design: Shan Fang, Lan Yang; analysis and interpretation of results: Shan Fang, Shoucai Jing; draft manuscript preparation: Shan Fang, Tianqi Wang. All authors reviewed the results and approved the final version of the manuscript.

Acknowledgments

This research was funded by Natural Science Foundation of China (61703053) and China Postdoctoral Science Foundation Funded Project (2017M623091). We thank the previous paper "Analysis of Traffic Oscillation Mechanism and Harmonization Method of Speed Optimization at Signalized Intersection," which is published in the 19th COTA International Conference of Transportation. We also thank Dr. Xiangmo Zhao, Fei Hui, Zhigang Xu who are contributors to our research.

References

[1] H. Rakha and R. K. Kamalanathsharma, "Eco-driving at signalized intersections using V2I communication," in *14th International IEEE Conference on Intelligent Transportation Systems (ITSC)*, IEEE, Washington, DC, USA, 2011.

[2] B. Liu, Q. Shi, Z. Song, and A. El Kamel, "Trajectory planning for autonomous intersection management of connected vehicles," *Simulation Modelling Practice and Theory*, vol. 90, pp. 16–30, 2019.

[3] H. Yang, H. Rakha, and M. Ala, "Eco-cooperative adaptive cruise control at signalized intersections considering queue effects," *IEEE Transactions on Intelligent Transportation Systems*, vol. 18, no. 6, pp. 1–11, 2017.

[4] H. Yao, J. Cui, X. Li, Yu Wang, and S. An, "A trajectory smoothing method at signalized intersection based on individualized variable speed limits with location optimization," *Transportation Research Part D: Transport and Environment*, vol. 62, pp. 456–473, 2018.

[5] X. Qu, S. Wang, and J. Zhang, "On the fundamental diagram for freeway traffic: a novel calibration approach for single-regime models," *Transportation Research Part B: Methodological*, vol. 73, pp. 91–102, 2015.

[6] X. Qu, J. Zhang, and S. Wang, "On the stochastic fundamental diagram for freeway traffic: model development, analytical properties, validation, and extensive applications," *Transportation Research Part B: Methodological*, vol. 104, pp. 256–271, 2017.

[7] M. Zhou, X. Qu, and X. Li, "A recurrent neural network based microscopic car following model to predict traffic oscillation," *Transportation Research Part C: Emerging Technologies*, vol. 84, pp. 245–264, 2017.

[8] C. Ding, X. Wu, G. Yu, and Y. Wang, "A gradient boosting logit model to investigate driver's stop-or-run behavior at signalized intersections using high-resolution traffic data," *Transportation Research Part C: Emerging Technologies*, vol. 72, pp. 225–238, 2016.

[9] M. Levin and D. Rey, "Conflict-point formulation of intersection control for autonomous vehicles," *Transportation Research Part C: Emerging Technologies*, vol. 85, pp. 528–547, 2017.

[10] X. Li, A. Ghiasi, Z. Xu, and X. Qu, "A Piecewise trajectory optimization model for connected automated vehicles: exact optimization algorithm and queue propagation analysis," *Transportation Research Part B: Methodological*, vol. 118, pp. 429–456, 2018.

[11] F. Zhou, X. Li, and J. Ma, "Parsimonious shooting heuristic for trajectory design of connected automated traffic part I: theoretical analysis with generalized time geography," *Transportation Research Part B: Methodological*, vol. 95, pp. 394–420, 2017.

[12] J. Ma, X. Li, F. Zhou, J. Hu, and B. B. Park, "Parsimonious shooting heuristic for trajectory design of connected automated traffic part II: computational issues and optimization," *Transportation Research Part B: Methodological*, vol. 95, pp. 421–441, 2017.

[13] X. Li, H. Medal, and X. Qu, "Connected infrastructure location design under additive service utilities," *Transportation Research Part B: Methodological*, vol. 120, pp. 99–124, 2019.

[14] Z. Xu, T. Wei, S. Easa, X. Zhao, and X. Qu, "Modeling relationship between truck fuel consumption and driving behavior using data from internet of vehicles," *Computer-Aided Civil and Infrastructure Engineering*, vol. 33, no. 3, pp. 209–219, 2018.

[15] A. Ghiasi, X. Li, and J. Ma, "A mixed traffic speed harmonization model with connected autonomous vehicles," *Transportation Research Part C: Emerging Technologies*, vol. 104, pp. 210–233, 2019.

[16] Y. Bichiou and H. Rakha, "Developing an optimal intersection control system for automated connected vehicles," *IEEE Transactions on Intelligent Transportation Systems*, vol. 20, no. 5, pp. 1–9, 2018.

[17] J. Lee and B. Park, "Development and evaluation of a cooperative vehicle intersection control algorithm under the connected vehicles environment," *IEEE Transactions on Intelligent Transportation Systems*, vol. 13, no. 1, pp. 81–90, 2012.

[18] H. Jiang, J. Hu, S. An, M. Wang, and B. B. Park, "Eco approaching at an isolated signalized intersection under partially connected and automated vehicles environment," *Transportation Research Part C: Emerging Technologies*, vol. 79, pp. 290–307, 2017.

[19] S. Jing, F. Hui, X. Zhao, J. Rios-Torres, and A. J. Khattak, "Cooperative game approach to optimal merging sequence and on-ramp merging control of connected and automated vehicles," *IEEE Transactions on Intelligent Transportation Systems*, vol. 20, no. 11, pp. 4234–4244, 2019.

[20] J. Ma, X. Li, S. Shladover et al., "Freeway speed harmonization," *IEEE Transactions on Intelligent Vehicles*, vol. 1, no. 1, pp. 78–89, 2016.

[21] S. Learn, J. Ma, K. Raboy, F. Zhou, and Y. Guo, "Freeway speed harmonisation experiment using connected and automated vehicles," *IET Intelligent Transport Systems*, vol. 12, no. 5, pp. 319–326, 2018.

[22] Y. Guo, J. Ma, C. Xiong, X. Li, F. Zhou, and W. Hao, "Joint optimization of vehicle trajectories and intersection controllers with connected automated vehicles: combined dynamic programming and shooting heuristic approach," *Transportation Research Part C: Emerging Technologies*, vol. 98, pp. 54–72, 2019.

[23] D. Hale, B. Park, A. Stevanovic, P. Su, and J. Ma, "Optimality versus run time for isolated signalized intersections," *Transportation Research Part C: Emerging Technologies*, vol. 55, pp. 191–202, 2015.

[24] W. Zhao, D. Ngoduy, S. Shepherd, R. Liu, and M. Papageorgiou, "A platoon based cooperative eco-driving model for mixed automated and human-driven vehicles at a signalised intersection," *Transportation Research Part C: Emerging Technologies*, vol. 95, pp. 802–821, 2018.

[25] Y. Feng, C. Yu, and H. Liu, "Spatiotemporal intersection control in a connected and automated vehicle environment," *Transportation Research Part C: Emerging Technologies*, vol. 89, pp. 364–383, 2018.

[26] M. Treiber, A. Hennecke, and D. Helbing, "Congested traffic states in empirical observations and microscopic simulations," *Physical Review E*, vol. 62, no. 2, pp. 1805–1824, 2000.

[27] K. Ahn, H. Rakha, A. Trani, and M. Van Aerde, "Estimating vehicle fuel consumption and emissions based on instantaneous speed and acceleration levels," *Journal of Transportation Engineering*, vol. 128, no. 2, pp. 182–190, 2002.

[28] G. Pinto and M. Oliver-Hoyo, "Using the relationship between vehicle fuel consumption and CO_2 emissions to illustrate chemical principles," *Journal of Chemical Education*, vol. 85, no. 2, p. 218, 2008.

[29] J. Sun, Z. Zheng, and J. Sun, "Stability analysis methods and their applicability to car-following models in conventional and connected environments," *Transportation Research Part B: Methodological*, vol. 109, pp. 212–237, 2018.

[30] M. Barth, S. Mandava, K. Boriboonsomsin, and H. Xia, "Dynamic ECO-driving for arterial corridors," *IEEE Forum on Integrated and Sustainable Transportation Systems*, 2011.

[31] M. Treiber and V. Kanagaraj, "Comparing numerical integration schemes for time-continuous car-following models," *Physica A: Statistical Mechanics and its Applications*, vol. 419, pp. 183–195, 2015.